Astronomy & Astrophysics

CHANG-ES

XXVI. Insights into cosmic-ray transport from radio halos in edge-on galaxies[*]

M. Stein[1], V. Heesen[2], R.-J. Dettmar[1], Y. Stein[1], M. Brüggen[2], R. Beck[3], B. Adebahr[1], T. Wiegert[4],
C. J. Vargas[5], D. J. Bomans[1,6], J. Li[7,8], J. English[9], K. T. Chyży[10], R. Paladino[11],
F. S. Tabatabaei[12], and A. Strong[13]

[1] Ruhr University Bochum, Faculty of Physics and Astronomy, Astronomical Institute (AIRUB), 44780 Bochum, Germany
  e-mail: mstein@astro.ruhr-uni-bochum.de
[2] Hamburger Sternwarte, University of Hamburg, Gojenbergsweg 112, 21029 Hamburg, Germany
[3] Max-Planck-Institut für Radioastronomie, Auf dem Hügel 69, 53121 Bonn, Germany
[4] CSI – Instituto de Astrofísica de Andalucía, Glorieta de la Astronomía s/n, 18008 Granada, Spain
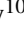[5] University of Arizona, Steward Observatory, 933 N Cherry Ave., Tucson, AZ 85721, USA
[6] Ruhr-Universität Bochum, Research Department, Plasmas with Complex Interactions, 44780 Bochum, Germany
[7] Department of Astronomy, University of Michigan, 311 West Hall, 1085 South University Avenue, Ann Arbor, MI 48109, USA
[8] Purple Mountain Observatory, Chinese Academy of Sciences, 10 Yuanhua Road, Nanjing 210023, PR China
[9] University of Manitoba, Dept of Physics and Astronomy, Winnipeg, Manitoba R3T 2N2, Canada
[10] Astronomical Observatory, Jagiellonian University, ul. Orla 171, 30-244 Kraków, Poland
[11] INAF – Istituto di Radioastronomia, Via P. Gobetti 101, 40129 Bologna, Italy
[12] School of Astronomy, Institute for Research in Fundamental Sciences, 19395-5531 Tehran, Iran
[13] Max-Planck-Institut für extraterrestrische Physik, Gießenbachstraße 1, 85748 Garching, Germany

ABSTRACT

Context. Galactic winds play a key role in regulating the evolution of galaxies over cosmic time. In recent years, the role of cosmic rays (CRs) in the formation of the galactic wind has increasingly gained attention. Therefore, we use radio continuum data to analyse the CR transport in edge-on galaxies.

Aims. With newly reduced radio continuum data of five edge-on galaxies (NGC 891, NGC 3432, NGC 4013, NGC 4157, and NGC 4631), we plan to set new constraints on the morphology of radio halos and the physical properties of galactic winds driven by stellar feedback. By distinguishing between the central and outer regions of the galaxies, our study setup allows us to search for variations in the radio halo profile or CR transport along the galactic disk.

Methods. Data from the LOFAR Two-metre Sky Survey (LoTSS) Data Release 2 at 144 MHz (HBA) and reprocessed data from the Very Large Array (VLA) at 1.5 GHz (*L* band) from the Continuum Halos in Nearby Galaxies – an EVLA Survey (CHANG-ES) enable us to increase the extent of the analysed radio continuum profile significantly (up to a factor of 2) compared to previous studies. We computed thermal emission maps using a mixture approach with Hα and near-infrared data, which were then subtracted to yield radio synchrotron emission maps. Then we compiled non-thermal spectral index maps and computed intensity profiles using a box integration approach. Lastly, we performed 1D CR transport modelling.

Results. The non-thermal spectral index maps show evidence that the LoTSS maps are affected by thermal absorption in star-forming regions. The scale height analysis reveals that most of the galaxies are equally well fitted with a one-component instead of a two-component exponential profile. We find a bi-modality within our sample. While NGC 3432 and NGC 4013 have similar scale heights in the *L* band and HBA, the low-frequency scale heights of NGC 891, NGC 4157, and NGC 4631 exceed their high-frequency counterpart significantly. The 1D CR transport modelling shows agreement between the predicted magnetic field strength and the magnetic field strength estimates of equipartition measurements. Additionally, we find an increasing difference in wind velocities (with increasing height over the galactic disk) between the central and outer regions of the analysed galaxies.

Key words. galaxies: evolution – galaxies: halos – galaxies: star formation – cosmic rays – radio continuum: galaxies

1. Introduction

The evolution of galaxies is a highly complex and not yet fully understood process. The circumgalactic medium (CGM) builds the venue where most of the driving factors interplay. There are multiple processes that directly influence the CGM: gas is introduced by cosmic accretion of the intergalactic medium, satellite galaxies and their winds add gas from outside of the galaxy halo (cf. Hafen et al. 2019), thermal instabilities convert hot gas to cold (cf. Butsky et al. 2020), and galactic winds of the host galaxy itself also transport gas from the disk into its halo. The constituents of this interplay need to be analysed separately and discussed together in order to derive a holistic view. Analyses of the CGM show that the CGM fuels the galaxy's star formation and moderates feedback processes (Tumlinson et al. 2017). Therefore, analysing details of the CGM (e.g. multi-phase

structure, gas dynamics, and metallicity) is key to a better understanding of the evolution of galaxies. In addition to all these dynamical and thermal processes, simulations show that there are also non-thermal processes such as magnetic fields and cosmic rays (CRs) that directly influence the CGM (cf. Ji et al. 2020; van de Voort et al. 2021). In this article we focus on galactic winds of the host galaxy that drive the processed interstellar medium (ISM) into the galactic halo.

In recent years, CRs have gained increasing attention from observers as well as theorists, as their influence on the ISM and galactic evolution in general might have been overlooked before. The interactions of CRs with the ISM are manifold and complex. Cosmic rays propagate from their origin, supernova (SN) remnants, through the galactic disk and into the galactic halo. Several propagation mechanisms can operate in this environment, namely advection, diffusion, and streaming (Strong et al. 2007; Butsky & Quinn 2018; Quataert et al. 2022a,b). Cosmic rays interact mainly with the galactic magnetic field and can therefore transfer some of their momentum to the thermal gas through scattering in magnetic field irregularities with the force directed down the CR pressure gradient. This then leads to a fluid description of the interaction between CRs and thermal gas and is sometimes referred to as 'cosmic ray hydrodynamics' (Zweibel 2017). In this context, the cosmic ray electrons (CREs) are used as proxies for the whole CR population – both CREs and cosmic ray protons (CRPs) – which peaks at a few GeV. This is motivated by the similar shape of the CRE and CRP spectra[1]. This hydrodynamic description has been implemented in galactic wind models that show that the mass-loss rate, gaseous distribution, and even the existence of winds are dependent on CR transport (e.g. Breitschwerdt et al. 1991; Everett et al. 2008; Uhlig et al. 2012; Salem & Bryan 2014; Recchia et al. 2016; Girichidis et al. 2016). It is the properties (i.e. wind speed and implied magnetic field strength in the galactic halo) of these winds, driven by stellar feedback, that we explore further in this work.

Radio continuum observations offer us the possibility to study the transport of CRs using the electrons as a tracer (see Heesen 2021, for an overview). With the non-thermal component of the radio continuum emission, one can follow CREs from their origin, SNe in star-forming regions, into the galactic halo. On their way through the galaxy, these charged particles gyrate around the magnetic field lines and therefore emit synchrotron radiation. Among the questions we would like to answer are whether these winds exist in the first place, and if so, whether they are able to overcome the galactic gravitational potential and therefore enrich the CGM. Edge-on spiral galaxies are good laboratories for studying galactic winds because only here can the path of the galactic wind into the halo be examined. Wiegert et al. (2015) show that such radio halos can be detected using deep radio continuum data; they even detected radio halos with vertical extents larger than the diameter of the disk. Tumlinson et al. (2017) note that the CGM reaches several hundred kiloparsecs (kpc; based on absorption studies). Such a scale cannot be probed with today's radio continuum observations. Here, the emission reaches about 10 kpc (e.g. Heald et al. 2022). However, as pointed out before, the analysis of these galactic winds is very important for a better understanding of the CGM properties since the material of the galactic disk can

only reach the CGM if and only if a bona fide wind develops. Since synchrotron radiation preferably depletes the highest energy electrons, the non-thermal SPectral IndeX (SPIX) of the emission is expected to steepen on its way from the disk into the galaxy halo. This steepening of the radio spectrum is usually referred to as spectral ageing. The SPIX α ($I_\nu \propto \nu^\alpha$) in this work is defined as

$$\alpha = \frac{\log{(S_{\nu_1}/S_{\nu_2})}}{\log{(\nu_1/\nu_2)}}. \tag{1}$$

Such a steepening is observed in radio galaxies (e.g. Carilli & Barthel 1996; Heesen et al. 2018a) as well as in star-forming galaxies (e.g. Schmidt et al. 2019; Mora-Partiarroyo et al. 2019; Miskolczi et al. 2019; Stein et al. 2019a; Heald et al. 2022). For star-forming galaxies, the steepening of the SPIX can be used to further analyse the transport of CRs in galactic winds. As CRs are accelerated by SNe in the galactic disk, there is a gradient in the CR pressure pointing from the galactic disk into the halo. As pointed out by Recchia et al. (2016) and Heald et al. (2022), this gradient influences the background plasma by adding an additional pressure term, P_{CR}, to the overall pressure, which can exceed the gravitational pull and therefore launch a CR-driven wind.

The use of low-frequency radio data to analyse non-thermal galactic winds via CR ageing offers a twofold advantage. First, for such an analysis, a reliable SPIX measurement is essential. From Eq. (1), one can deduce that the accuracy of the SPIX measurement grows with the relative distance of the two analysed spectral bands. Therefore, combining low- and high-frequency datasets increases the quality of the SPIX measurement (Strong 1978; Miskolczi et al. 2019; Stein et al. 2019a). Second, with low-frequency data one can trace the older CR population that has already travelled far into the galactic halo, which therefore increases the extent to which the halo is observable. On the basis of such datasets (high- and low-frequency radio continuum maps), one can reliably determine whether advection or diffusion is the dominant transport mechanism. Advection-dominated transport seems to produce large radio halos, while diffusion-dominated transport results in much smaller halos (cf. Heesen et al. 2016; Stein et al. 2019b).

To conclude this section, we note that the importance of CRs for the galactic winds and for the evolution of galaxies as a whole is now widely recognised. However, the interaction of CRs with the ISM and the galactic magnetic field are not yet understood in detail. In particular, the potential of CRs to drive galactic winds is the subject of ongoing discussion. A crucial observational experiment would be to measure both the outflow velocity of the ionised gas and the CR advection speed. With CR-driven winds, we would expect the CRs to be transported faster than the gas, which is the basic mechanism that can offset the adiabatic cooling of the gas in the hydrodynamic model of CR-driven winds (Zweibel 2017). Such a differential velocity could be explained, for instance, by CR streaming with the Alfvén velocity or by CR diffusion down the density gradient (Wiener et al. 2017). Observationally, this is a difficult task as it is hard to measure both velocities due to geometry. While edge-on galaxies allow us to study the radio halo and the CR advection speed, face-on galaxies are better suited for studying outflow speeds of the ionised gas with optical or ultraviolet spectroscopy (Heckman et al. 2015). Therefore, as an alternative, we aim to build a coherent picture of both CR and gaseous transport in galactic halos in a sample of galaxies with similar properties over a range of fundamental parameters in order to better

---

[1] The CRPs have a much higher energy density than CREs but due to the higher rest mass of the protons, CRPs with energies of a few GeV are not observable because they emit most of their synchrotron radiation at very low and therefore non-observable frequencies (Zweibel 2013).
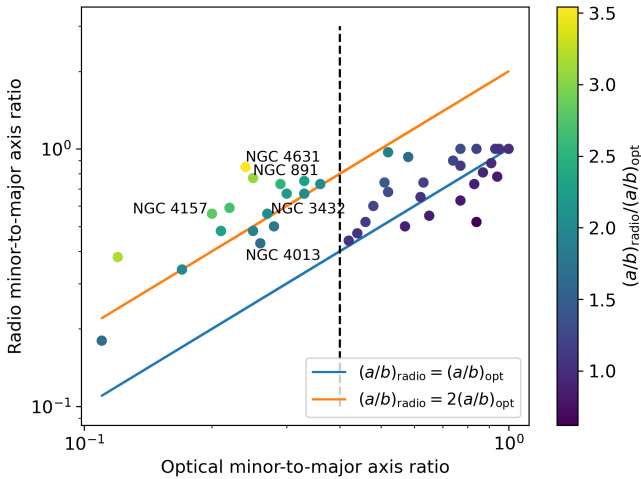
Fig. 1. Minor-to-major axis ratios in the radio continuum and optical light. Data points are from LoTSS DR2, and CHANG-ES galaxies are located to the left of the vertical dashed line. Data points are coloured according to their radio-to-optical axis ratios. Radio halos are particularly prominent if $(a/b)_{radio} \geq 2(a/b)_{opt}$, as indicated by the orange line.

understand the influence of CR transport mechanisms on stellar-feedback-driven winds (see Heesen 2021, for a review). Expanding this picture with new deep radio observations is the goal of this work.

This paper is structured as follows: In Sect. 2 we describe the galaxies that are analysed in this work and put them into context by comparing them to other nearby galaxies. Section 3 describes the data that are used, and Sect. 4 describes the processing of the data. We then present the first results in Sect. 5 before further analysing the radio halo profiles in Sect. 6 and deriving the physical properties of the non-thermal galactic wind by applying a 1D CR transport model in Sect. 7. Lastly, we conclude the paper in Sects. 8 and 9.

2. Sample description

The orientation of the galaxy is an important factor when analysing the interaction of the galactic disk with its halo. Edge-on galaxies allow us to trace the CREs from their origin in the disk over several kpc into the galaxy halo. Therefore, the data acquired for the Continuum Halos in Nearby Galaxies – an EVLA Survey (CHANG-ES), is the starting point for our analysis. The CHANG-ES survey consists of 35 nearby ($d \leq 42$ Mpc) edge-on ($76° \leq i \leq 90°$) galaxies (Irwin et al. 2012; Wiegert et al. 2015). As previously outlined, adding low-frequency data to the information drawn from the radio maps obtained with the Very Large Array (VLA) highly improves the quality of SPIX maps, which is a crucial for the planned analysis. Therefore, we only chose the 17 galaxies that lie in the footprint of the LOFAR Two-metre Sky Survey (LoTSS) Data Release 2 (DR2).

Radio halos of edge-on galaxies can be identified by comparing the minor-to-major axis ratios in the radio continuum and optical emission. If a radio halo is present, we expect the ratio in the radio continuum to be significantly larger than the optical one. In Fig. 1, we show such a comparison for the LoTSS DR2 sample. As the CHANG-ES galaxies have high inclination angles, they lie on the left side of the plot, clearly separated from the other galaxies with moderate inclination angles. We find that of the 17 CHANG-ES galaxies in

LoTSS DR2, nine galaxies have axis ratios with $(a/b)_{radio} \gtrsim 2(a/b)_{opt}$. These galaxies are NGC 2820, NGC 4157, NGC 5297, NGC 3079, NGC 4631, NGC 891, NGC 3556, NGC 2683, and NGC 4217 (listed with increasing $(a/b)_{opt}$). Hence, these galaxies are most promising to study galactic winds. Of these galaxies, two were studied previously with LOFAR, namely NGC 891 (Mulcahy et al. 2018) and NGC 3556 (Miskolczi et al. 2019), where CR transport was specifically modelled only in NGC 3556. Of the remaining galaxies, NGC 4631, NGC 891, NGC 2820, and NGC 4157 have the highest radio-to-optical ratios. We chose to omit NGC 2820 as previous analyses (e.g. van der Hulst & Hummel 1985; VLA 1.5 GHz), Wiegert et al. (2015; CHANG-ES D configuration), Irwin et al. (2019; CHANG-ES B-configuration), Kantharia et al. (2005; GMRT), and 2022b (Heesen et al.; LoTSS)) show a strong radio bridge, reaching from the galaxy to its closest interaction partner NGC 2814, which will most probably disturb the radio halo and therefore prevent the planned analysis. As NGC 891 and NGC 4157 are fairly fast rotating, compared to NGC 4631, we decided to also include NGC 3432, which has a less prominent radio halo, to have another slow rotating galaxy in our sample. We further include NGC 4013, which was already studied by Stein et al. (2019a) who found a diffusion-dominated radio halo. We chose to re-analyse this galaxy with consistent methods, as we expect a more accurate measurement of the radio halo intensity profile due to the newly processed datasets. Hence, we chose five galaxies from LoTSS DR2 for further analysis, namely NGC 891, NGC 3423, NGC 4013, NGC 4157, and NGC 4631. Table 1 lists some fundamental parameters of each analysed galaxy.

3. Data

3.1. Radio continuum data

In order to avoid losses of diffuse emission in these extended galaxies and their halos, we combine C-configuration and D-configuration L-band data. All VLA datasets that are used in this project where observed for the CHANG-ES project (Project Code 10C-119). The observation and calibration strategy is fully described for the D-configuration data in Wiegert et al. (2017)[2]. In Table 2, we list the relevant information for the VLA C-configuration L-band observations. Phase and flux density calibration have been performed using the `Common Astronomy Software Applications package` (CASA; McMullin et al. 2007). Self-calibration was incorporated in the calibration process if it increased the data quality. The frequency range for all targets spans from 1.247 GHz to 1.503 GHz and from 1.647 GHz to 1.903 GHz. Cleaning is performed using `WSClean` (Offringa et al. 2014). We incorporate multi-scale cleaning, automatic masking and a Briggs robust weighting of 0.4. Additionally, a Gaussian taper of 6″ is applied to the uv-weights and the restoring beam size is set to 20″.

The LOFAR data are based on observations from LoTSS (Shimwell et al. 2017, 2019), specifically data from LoTSS DR2 (Shimwell et al. 2022). These data are taken with the high-band antenna (HBA) system with an effective frequency of 144 MHz. The data were presented in Heesen et al. (2022b), the data release paper of nearby galaxies in LoTSS DR2. Besides following standard observing and data reduction procedures for LoTSS data as described by Shimwell et al. (2017, 2019), we used the

---

Table 1. Fundamental information about the galaxies analysed in this work.

Galaxy	RA [H:M:S]	Dec [D:M:S]	Morph. Type	PA [°]	Incl. [°]	Distance [Mpc]	Diam. [kpc]	v_{rot} [km s^{-1}]	$M_{baryonic}$ [$M_\odot$] $\times 10^{10}$
NGC 891	02h22m33.41s	+42d20m56.9s	Sb	22.0	90.0	9.1	25.1	212	8.63
NGC 3432	10h52m31.13s	+36d37m07.6s	SBm	33.0	85.0	9.4	9.96	110	0.86
NGC 4013	11h58m31.380s	+43d56m47.70s	SABb	58.6	88.0	16	16.1	182	4.99
NGC 4157	12h11m04.37s	+50d29m04.8s	SABb	64.7	83.0	15.6	16.6	189	5.75
NGC 4631	12h42m08.01s	+32d32m29.4s	SBcd	85.7	85.0	7.4	23.4	139	1.93

Notes. Celestial coordinates at epoch J2000.0 [a], morphological type [b], position angle [b], inclination [c], distance [d], diameter (based on 22 µm WISE map) [d], rotational velocity [c], and total baryon mass [e]. [a]Taken from the NASA NED (https://ned.ipac.caltech.edu/). [b]Taken from the HyperLeda Database (http://leda.univ-lyon1.fr/). [c]Taken from Heesen et al. (2022b). [d]Taken from Wiegert et al. (2015). [e]Taken from Li et al. (2016).

Table 2. Basic information about the galaxies from EVLA C-Array observations.

Galaxy	Observing date [M-D-Y]	Integration time [M:S]	Flux cal.	Phase cal.	SB ID
NGC 891	02-11-2012, 04-01-2012	46:40	3C48	J0314+4314	8237609, 8182311
NGC 3432	03-25-2012	43:20	3C286	J1006+3454	8256114
NGC 4013	03-31-2012	44:00	3C286	J1219+4829	8318174
NGC 4157	03-31-2012	41:00	3C286	J1219+4829	8318174
NGC 4631	02-04-2012	77:00	3C286	J1221+2813	8312467

Table 3. Flux densities and map properties of the analysed sample.

Galaxy	Ellipse $a \times b$ [a] [arcmin^2]	S_{HBA} [Jy]	σ_{HBA} [µ Jy/Beam]	$S_{L\text{-Band}}$ [Jy]	σ_{Lband} [µ Jy/Beam]	d_{HBA}^{disk} [kpc]	d_{HBA}^{halo} [kpc]
NGC 891	5.9 × 4.55	3.3±0.3	207	0.68±0.03	31	28.4	15.6
NGC 3432	4.35 × 2.2	0.30±0.03	165	0.086±0.004	22	14.4	8.5
NGC 4013	2.36 × 1.45	0.151±0.015	167	0.0381±0.0019	34	16.1	5.4
NGC 4157	4.25 × 2.08	1.01±0.10	196	0.180±0.009	35	34.8	21.7
NGC 4631	8.8 × 7.5	4.46±0.45	235	1.03±0.05	25	30.0	24.6

Notes. We list the integrated flux density measurements in HBA (S_{HBA} and L band ($S_{L\text{-Band}}$), based on the described aperture, accounting for background noise (σ_{HBA} & $\sigma_{L\text{-Band}}$) as well as calibration errors. Physical diameters, based on the 3σ contours in HBA, parallel (d_{HBA}^{disk}) and orthogonal (d_{HBA}^{halo}) to the galactic disk are also listed. [a]Ellipses are defined in Heesen et al. (2022b) and encompass the 3σ contours of the re-calibrated LoTSS map.

re-calibration pipeline described by van Weeren et al. (2021), which results in new (u, v) datasets that are specifically tailored to our target galaxies. The maps are CLEANed using WSClean with a Briggs weighting of −0.25 and a Gaussian taper of 10″ with a fixed restoring beam size of 20″ (see Heesen et al. 2022b, for further information). The imaging process of NGC 891 was challenging due to its proximity to a ∼10 Jy radio source (at 1.4 GHz; Kellermann et al. 1969), the radio galaxy 3C 66, and some fine tuning of parameters was necessary. Therefore, we use a slightly different strategy when creating a new 144 MHz map for NGC 891 with WSClean. Here, we incorporate a Briggs weighting of −0.15 together with multi-scale CLEAN. In order to accurately account for the influence of 3C 66, which lies to the north of NGC 891, the map spans over ∼1.9° × 1.9°. A Gaussian taper of 7″ is applied in the (uv)-plane and the final beam size is set to 20″. This map has also been published by Heesen et al. (2022b). To estimate the noise levels of all radio maps, we ran PyBDSF (Mohan & Rafferty 2015), using standard parameters (source detection threshold 5σ; island boundary threshold 3σ). The resulting noise estimates are listed in Table 3.

3.2. Additional datasets

As in Vargas et al. (2018), we used resolution enhanced (12″4) WISE 22 µm images to correct for thermal emission in our CHANG-ES galaxies (Jarrett et al. 2012, and T. Jarrett, priv. comm.), combined with Hα data. Since the resulting WISE point spread function (PSF) may deviate significantly from a purely Gaussian PSF, we used an empirical PSF model when convolving the maps to the resolution of the radio maps (Jarrett et al. 2019). This model was compiled by stacking stars in a large field to extract the shape of the PSF (Jarrett et al. 2019). Hα images of all CHANG-ES galaxies have been analysed in Vargas et al. (2019). For this analysis, 25 of the 35 CHANG-ES galaxies (including NGC 3432, NGC 4013, and NGC 4157) were observed with the 3.5 m telescope of the Apache Point Observatory (see Vargas et al. 2019, for further information). For NGC 4631, Vargas et al. (2019) use an Hα map that was observed with the 2.1 m telescope at the Kitt Peak National Observatory as ancillary data for the *Spitzer* Infrared Nearby Galaxies Survey (SINGS; Daigle et al. 2006; Dicaire et al. 2008). The Hα map of NGC 891 was obtained

from the ancillary dataset for the Westerbork Synthese Radio Telescope (WSRT) Hydrogen Accretion in LOcal GAlaxieS (HALOGAS) survey (Heald et al. 2011, Heald & HALOGAS Team in prep.).

4. Method

4.1. Point source removal

In order to extract the radio profile, background and foreground point-like sources need to be removed. We detect compact sources by using PyBDSF with an adaptive_rms_box and a maximum detection island size. The detected sources are then fitted as Gaussian components and subtracted from the original image. Only large, extended sources remain in the residual image.

We further inspect the images manually to mask out previously undetected or nested sources by using the corresponding LoTSS 6″ map, published in Heesen et al. (2022b), for an exact positioning of the masks. With this approach, the profile of the galaxy can be reliably followed, without being affected by back- or foreground sources.

4.2. Thermal correction

In star-forming galaxies, radio continuum emission is a superposition of thermal and non-thermal processes:

$$S_{tot}(\nu) = S_{th}(\nu_0)\left(\frac{\nu}{\nu_0}\right)^{-0.1} + S_{nth}(\nu_0)\left(\frac{\nu}{\nu_0}\right)^{\alpha_{nth}}, \qquad (2)$$

where S denotes the flux density at a given frequency ν_0. The standard picture is that the thermal emission follows a power-law with a SPIX of -0.1. Overall, the measured combined SPIX is about $\alpha_{tot} \approx -0.7$. Therefore, in order to analyse non-thermal processes such as winds driven by stellar feedback, the thermal emission needs to be estimated and subtracted. However, from Eq. (2), one can deduce that the fraction of the thermal emission drops when reaching lower frequencies and hence that such a correction might not be needed for low-frequency data. It is also important to note that there are significant deviations from a constant non-thermal SPIX when reaching higher frequencies (Klein et al. 2018). In the literature, there are several approaches to separate the synchrotron emission from the thermal emission, for example assuming a constant non-thermal SPIX (Klein et al. 1982), estimating the thermal emission from H II regions (Beck & Graeve 1982), or using de-reddened Hα emission (Tabatabaei et al. 2007, 2018).

For this project, we re-implemented[3] the mixture-method technique developed by Vargas et al. (2018), which is specifically designed to estimate the thermal emission in edge-on galaxies. This technique is based on the combination of Hα and mid-infrared (WISE 22 μm) images to compile a star formation map and then convert this map to a thermal emission map. This technique also has been applied in the second CHANG-ES data release paper (Vargas et al. 2019). For in depth details of the technique, we refer to Vargas et al. (2018, 2019).

Here, we shortly describe the overall workflow and point out where we deviate from the current implementation. In order to combine Hα with mid-infrared data and later apply them to a radio map, we first needed to match resolutions. As the mid-infrared images have a resolution of ~12″4 but deviate significantly from a Gaussian PSF, it is not advisable to convolve the

original images with a purely Gaussian kernel as the result will not be a Gaussian PSF. This is especially important when the target resolution of the radio maps is only slightly above the full width half maximum (FWHM) of the mid-infrared images. Therefore, it is imperative to use individually tuned homogenisation kernels. The former implementation used convolution kernels provided by Aniano et al. (2011), where one could select from a variety of kernels to produce a Gaussian PSF with a predefined FWHM. As this approach limits analyses to certain resolutions, we now use the WISE PSF model described in Sect. 3 and the Python package PyPHER[4] (Boucaud et al. 2016; Boucaud 2016) to convolve the mid-infrared image to the target resolution. The benefit of such an approach is that one can select any type of target kernel, rather than having to choose from a couple of pre-selected kernels. As the Hα observations are mainly seeing limited, their resolution is of the order of ~1″5. Since the target resolution of any study that uses the mid-infrared data needs to be above 12″4, the resulting PSF for the Hα image will be dominated by the convolution kernel, so that we can convolve the Hα images with a purely Gaussian kernel.

The resolution-matched and calibrated (erg s^{-1} cm^{-2}) images can then be further processed. As the following method relies on 24 μm data, the WISE band 4 data, which are centred on 22 μm, need to be corrected. As shown by Wiegert et al. (2015), there is a tight linear relationship between 22 μm and 24 μm emission and therefore, the data can be scaled using a factor of 1.03. Following Calzetti et al. (2007), we can use the mid-infrared data to correct the Hα maps for dust extinction:

$$L_{H\alpha\_corr} = L_{H\alpha\_obs} + 0.042 \cdot L_{24\mu m}. \qquad (3)$$

The factor 0.042 was derived in Vargas et al. (2018) and is only valid for edge-on or very dusty galaxies and corrects the original factor by Calzetti et al. (2007) with an additional factor of 1.36. The corrected Hα emission can then be related to a star formation rate (SFR) and hence to the thermal radio emission at a frequency, ν (Murphy et al. 2011; Vargas et al. 2018):

$$SFR_{mix} [M_\odot/yr] = 5.37 \times 10^{-42} \cdot L_{H\alpha\_corr\,[erg\,s^{-1}]}, \qquad (4)$$

$$L_\nu^T [erg\,s^{-1}\,Hz^{-1}] = 2.2 \times 10^{27} \left(\frac{T_e\,[K]}{10^4}\right)^{0.45} \left(\nu\,[GHz]^{-0.1}\right) SFR_{mix}. \qquad (5)$$

Here, we assume an average electron temperature of $T_e = 10^4$ K (Osterbrock & Ferland 2006; Calzetti et al. 2007). With Eq. (5) we compute thermal emission maps for 144 MHz as well as for 1.5 GHz. These thermal maps can then be subtracted from the radio maps to obtain the pure synchrotron emission.

As a concluding remark, we note that several assumptions and systematic uncertainties influence the estimate of the thermal emission (e.g. a varying Hα/N [II] ratio in the diffuse ionised gas Otte & Dettmar 1999), which makes accounting for N [II] contamination in the Hα images more complicated, or varying electron temperatures) that dominate the statistical uncertainties coming from the Hα and mid-infrared background noises. Vargas et al. (2018) present a detailed analysis of all relevant factors and conclude that the thermal emission estimates have an overall uncertainty of approximately 14%. Considering the fact that the contribution of thermal emission to the overall radio emission in the L band in the observed galaxies is of the order of approximately 30% in star-forming regions, the introduced uncertainties onto the radio data are expected to be approximately 4% (even less than the HBA data) and are therefore smaller than standard calibration errors.

---

[3] The Python3 package can be downloaded via https://github.com/msteinastro/thermal_maps_chang-es-xxvi

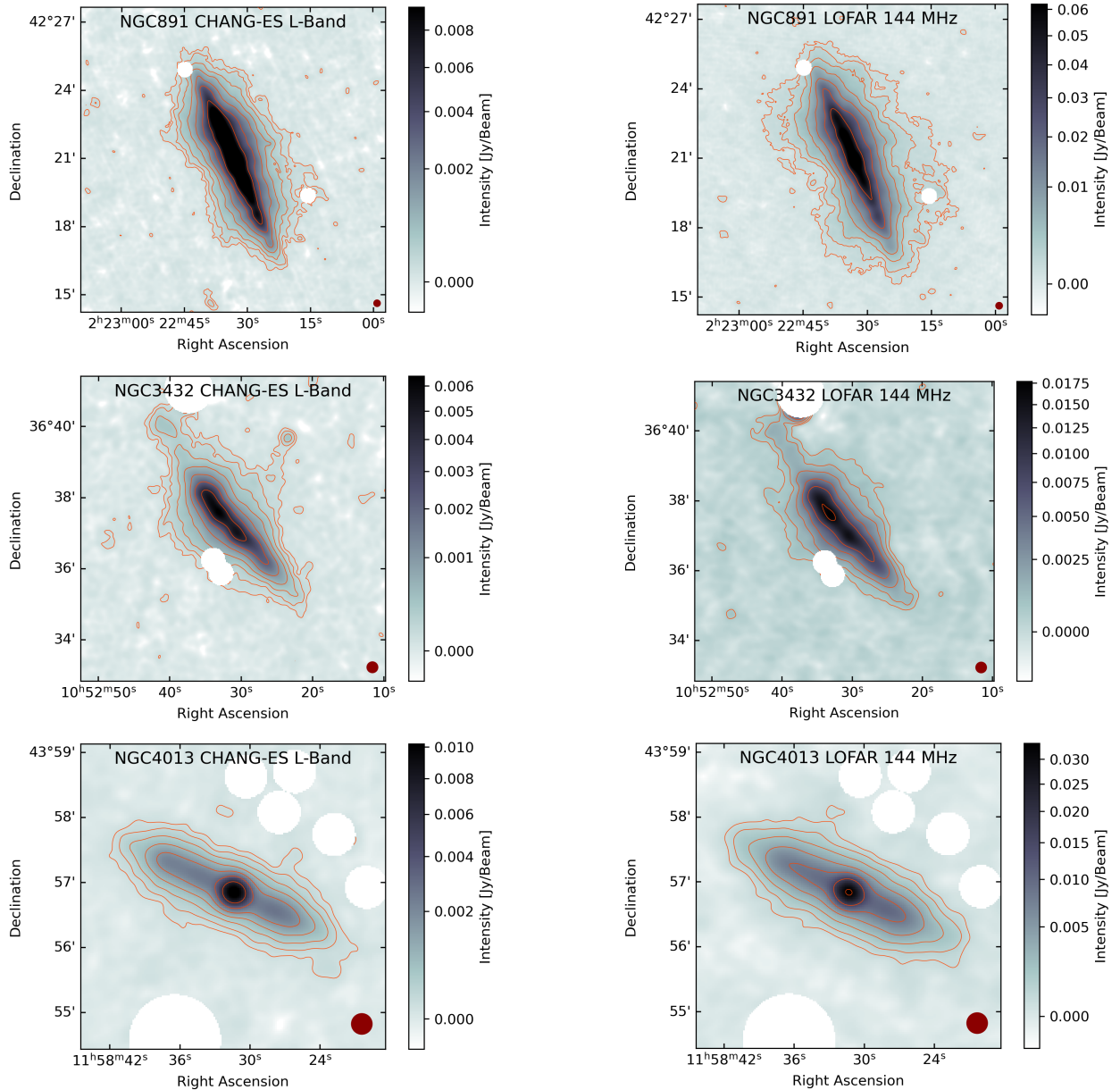[4] https://github.com/aboucaud/pypher

Fig. 2. Total intensity maps + contours from the CHANG-ES L band (left column) and LOFAR HBA (right column) after subtracting or masking point sources in the vicinity of the galaxy for NGC 891 (top row), NGC 3432 (middle row), and NGC 4013 (bottom row). Contours start at 3σ above the background noise and are in increments of 2. The beam is displayed in the bottom-right corner of each map as a dark red circle.

5. Results

5.1. Total intensity

Table 3 lists the integrated flux density measurements as well as the noise estimates for all analysed galaxies in the LOFAR HBA and VLA (CHANG-ES) L band. The uncertainties of the flux density measurements Δ_{S_ν} with a flux density of S_ν, are computed via

$$\Delta_{S_\nu} = \sqrt{\left(\sigma\sqrt{N_{\text{beams}}}\right)^2 + (\epsilon S_\nu)^2}. \tag{6}$$

Here, σ denotes the background noise of the individual map and N_{beams} the number of telescope beams that fit into the defined aperture. As an additional error term, one needs to account for calibration errors. This is implemented as a relative error term by setting $\epsilon = 0.1$ for the HBA measurements (Shimwell et al. 2017)

and setting $\epsilon = 0.05$ for the L-band measurements. Calibration errors are typically much more severe in the low-frequency regime; that is why we chose different weightings for the relative error terms. Since all the galaxies analysed in this work are relatively bright, the error terms are dominated by the calibration error rather than the background noise. In Figs. 2 and 3, we present the radio maps after the subtraction and masking of background or foreground sources. All galaxies show a distinct extent orthogonal to the galactic disk. Comparing the extent of the outermost (3σ) contour, we detect larger extents in the HBA maps compared to the L-band contours (for NGC 3432, this comparison is more challenging as the overall structure of the contours is more complex compared to the other galaxies). Of course, comparing the outermost contours is not a perfect way to determine the extent of a radio halo, as this measurement is limited only by the sensitivity of the particular dataset. However, one can already assume that this larger extent in the lower-frequency
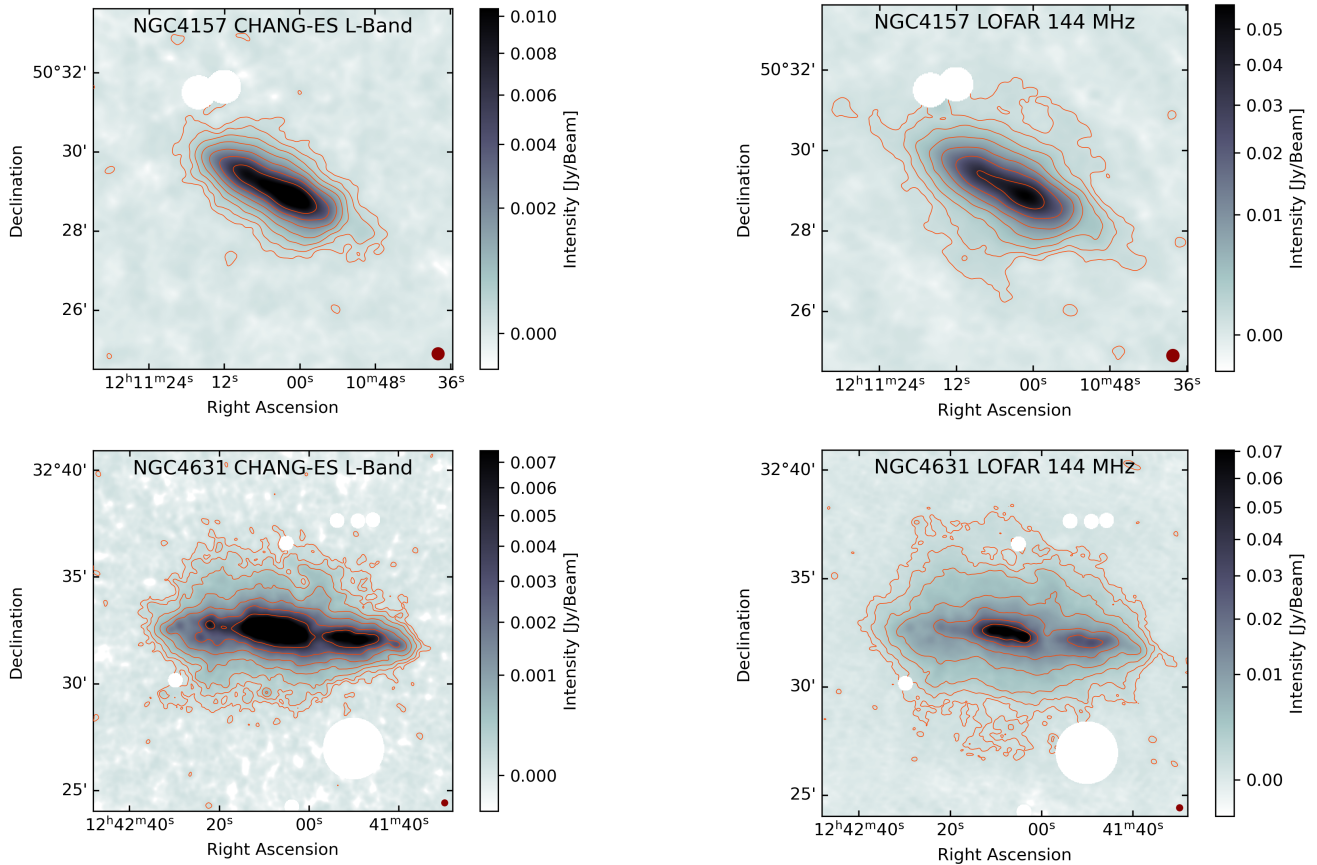
Fig. 3. Continuation of Fig. 2. Total intensity maps from the CHANG-ES *L* band (left column) and LOFAR HBA (right column) after subtracting or masking point sources in the vicinity of the galaxy for NGC 4157 (top row) and NGC 4631(bottom row).

dataset reflects the ageing process of the CREs. Another interesting point to discuss is that the size of the individual radio halos varies strongly between the galaxies when compared to the galaxy's major axis. This is best observed in the low-frequency maps. The physical extents of the galactic disk and the halo based on the 3σ contours of the HBA maps are listed in Table 3. While the radio halo of NGC 4013 shows only a small extent in the *z* direction, the radio halos of NGC 891, NGC 3432, and NGC 4157 reach already far up into the galactic halo. The most extreme case in this sample is certainly NGC 4631. Here, the extent in the *z* direction almost exceeds the galaxy's major axis. Such a comparison between the galaxies can be made because all LOFAR maps have a similar background noise (cf. Table 3). At this point, we can conclude that the dominating CRE transport mechanisms of the galaxies studied here are different. In a previous study, Stein et al. (2019a) have shown that the intensity and SPIX profiles of NGC 4013 might best be modelled with a diffusion-dominated CRE transport, which might result in a smaller vertical extent of the galactic halo.

5.2. Thermal and non-thermal emission

Here we present the result of the thermal emission correction, using the mixture method approach described in Sect. 4. Table 4 lists the integrated thermal flux densities integrated over defined aperture as well as the fraction of non-thermal emission (NTF), which is the remaining synchrotron radiation. As expected, the contribution of thermal emission to

Table 4. Integrated thermal flux densities and non-thermal fractions in the analysed sample.

Galaxy	$S_{\mathrm{HBA^{th}}}$ [Jy]	$S_{L-\mathrm{Band^{th}}}$ [Jy]	$\mathrm{NTF_{HBA}}$	$\mathrm{NTF}_{L\text{-Band}}$
NGC 891	0.056	0.044	0.98	0.94
NGC 3432	0.013	0.010	0.95	0.86
NGC 4013	0.006	0.005	0.96	0.86
NGC 4157	0.018	0.014	0.98	0.93
NGC 4631	0.117	0.092	0.97	0.91

the total radio emission decreases when lower frequencies are reached.

As an integrated value, the thermal emission in the *L* band is of the order of magnitude of the uncertainty due to the calibration error. However, the importance of the thermal emission changes when looking at the resolved fraction of thermal emission. To keep this work concise, we refer the reader to Appendix A for the thermal emission and thermal fraction maps. In the thermal fraction maps, one can see that both the intensity of the thermal emission and the fraction of thermal emission in the overall radio emission decrease strongly when leaving the galactic disk. In *L* band the thermal emission constitutes ~30% of the overall observed radio emission in the galactic disk (for NGC 4631, the thermal contribution reaches even up to ~40% in the galactic disk). However, the thermal fraction in the HBA data is much smaller. Here, the thermal emission normally does not exceed
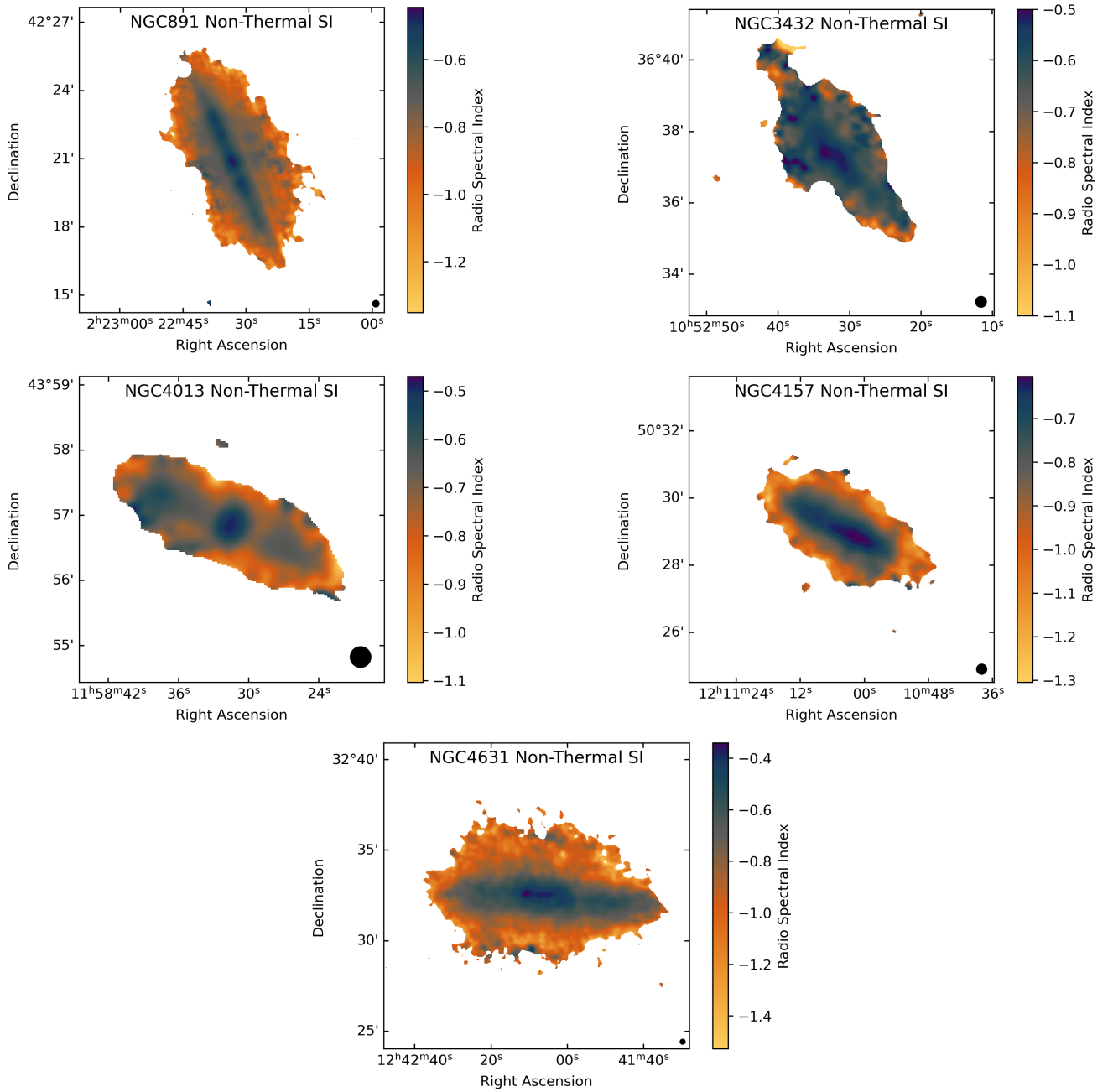
Fig. 4. Non-thermal SPIX maps (*L* band corrected for thermal emission and uncorrected HBA). We use a custom colour map, where a flat SPIX is coloured blue to plum and a steep SI orange to yellow. The beam is displayed in the bottom-right corner of each map as black circle.

10% of the total emission (only NGC 4631 shows some regions where the thermal fraction reaches 15%). Considering the overall calibration error of 10% in the LoTSS data, the effect of thermal emission does not seem to be significant at the observed frequency. Therefore, we decided to correct only the *L*-band data for thermal emission in the further analysis.

5.3. Spectral index

In Fig. 4 we present the non-thermal SPIX maps[5] for all analysed galaxies. As mentioned before, only the *L* band has been

corrected for thermal emission, since the thermal contamination in the HBA is not significant when considering calibration errors. Overall, the galaxies show a common trend. In the galactic plane, we detect a non-thermal SPIX of approximately −0.5. Similar values have been reported in studies of NGC 3556 (Miskolczi et al. 2019), NGC 5775 (Heald et al. 2022), and previous studies of NGC 891 (Schmidt et al. 2019), NGC 4013 (Stein et al. 2019a) and NGC 4631(Mora-Partiarroyo et al. 2019; Vijayan et al. 2022). NGC 4631 shows in the outer part of the galactic disk similar SPIX values compared to the other galaxies of our sample, but deviates from the other galaxies in the centre. Here, we report a SPIX of approximately −0.4. This area coincides with the region of highest star formation and thermal radio emission (cf. bottom-left map in Fig. 3). In Sect. 8.1 these results will be discussed in more detail.

---

5 Custom colour maps can be downloaded at: https://github.com/mlarichardson/CosmosCanvas/.

Table 5. Box widths (W) used for box integration, radio beam FWHM converted to physical scales, assumed flux tube radius (R_0) used for CR transport modelling for each galaxy; SFR, SFR surface density, and average equipartition magnetic field strength in the galactic disk for individual stripes; gravitational pull for central and outer stripes (as we assume the gravitational potential to be symmetric, there is no distinction for left and right stripes).

Galaxy	W ['']	Beam [kpc]	R_0 [kpc]	SFR [$M_\odot$ yr^{-1}]			Σ_{SFR} [$M_\odot$ yr^{-1} kpc^{-2}]$\times 10^{-3}$			B-Field Strength [μ G]			Gravitational pull [N]$\times 10^{-10}$	
				left	middle	right	left	middle	right	left	middle	right	middle	outer
NGC 891	177	0.88	7.8	0.5	1.0	0.4	3.9	5.6	2.8	9.2	13.1	9.0	3.7	0.6
NGC 3432	102	0.91	4.6	0.2	0.3	0.1	3.7	4.2	1.1	8.6	10.2	6.7	1.6	0.3
NGC 4013	63	1.36	4.3	0.2	0.3	0.1	4.6	5.6	3.8	7.5	9.1	7.3	5.0	0.8
NGC 4157	120	1.51	9.0	0.2	1.3	0.2	1.3	5.5	1.2	8.1	13.1	7.4	2.5	0.4
NGC 4631	266	0.72	9.6	0.3	1.6	0.5	1.8	6.1	2.8	7.5	11.7	8.9	1.3	0.2

NGC 891, NGC 4157, and NGC 4631 show a strong and uniform gradient (declining SPIX) from the galactic disk into the halo. Such a gradient can be attributed to the ageing of CREs. In NGC 4013, we also detect a gradient in the non-thermal SPIX. However, we find an extended region in the centre of the galaxy with very flat SPIX values ($\alpha_{\mathrm{nth}} < -0.7$) and the gradient in the outer regions seems to be less prominent. The case of NGC 3432 is much less ordered. A gradient in the SPIX is not clearly visible and and only further analysis will show if CRE ageing is observable in this galaxy. However, one could have expected such a confused SPIX map, considering the fact that NGC 3432 is closely interacting with the dwarf galaxy UGC 5983[6]. Therefore, the dynamics of the galaxy might have disturbed the propagation of the CREs.

Another process that could explain the non-detection of a gradient in the SPIX is CR diffusion with a very strong energy dependence ($\mu = 1$)[7]. The theoretical implications for a $\mu = 1$ energy dependence of the CR diffusion is discussed in Bulanov & Dogel (1974). This transport type would lead to a homogeneous non-thermal SPIX map, as the effects of CR transport and CR ageing would counterbalance each other. However, a $\mu > 0.7$ would require extreme conditions of the ISM turbulence or CR energies of about 10^4 GeV (Lazarian & Xu 2021). By comparing their models to radio data, Bulanov & Dogel (1974) obtain a limit of $\mu < 0.4$ for the energy dependence of the CR diffusion. Blasi et al. (2012) report an energy dependence of $D(E) \propto E^{0.7}$ for the energy range $10\,\mathrm{GeV} < E < 200\,\mathrm{GeV}$[8]. For energies slightly below 10 GeV, recent studies point to an even weaker ($\mu \sim 0.3$) energy dependence or no energy dependence of the CR diffusion at all (Lazarian & Xu 2021; Dörner et al. 2023).

6. Vertical intensity profiles

6.1. Box integration and scale height fitting

To trace the synchrotron emission further into the galactic halo, we average horizontally over large areas of the galaxy. In the literature, there is some variety in the number of strips into which the integration areas are divided. While Heald et al. (2022) split up the galaxy into quadrants by choosing two vertical strips and

splitting those again into northern and southern strips, there are also more detailed approaches (e.g. Stein et al. 2019a: five strips, Schmidt et al. 2019: five and seven strips). The number of strips used is obviously dependent on the spatial extend of the target compared to the spatial resolution of the observation, and fewer strips makes it possible to follow the galaxy's profile a bit further. We place three strips on each galaxy (left, middle, right) and analyse the upper and lower sections separately. Therefore, each galaxy is split up into six strips: upper left (UL), upper middle (UM), upper right (UR), lower left (LL), lower middle (LM), and lower right (LR). Here, the idea is to average as much data as possible while accounting for the different conditions in the galaxy regions (e.g. stronger magnetic field in the centre of the galaxy; localised star formation regions, etc.). Separating the central part of the galaxy from the outer regions is very valuable for our study as we know from our Galaxy that active galactic nucleus activity can heavily influence the galactic halo (e.g. *Fermi* bubbles; Su et al. 2010). Box integration is performed using the `BoxModels` method of `NOD3`[9] (Müller et al. 2017a,b). We use the 3σ contour of the HBA map as outline for defining the width of the boxes. The box setup for all galaxies is described in Table 5. Concerning the box height, we follow the approach of Krause et al. (2018) and Stein et al. (2019a) and set it to half of the beam width. As an example, we show the box setup for NGC 891 on the HBA map in Fig. 5.

In order to derive reliable scale heights for each strip, we fit each strip with four models of decreasing complexity and evaluate the Akaike information criterion (AIC; Akaike 1998) to select the best-fitting model while accounting for the different model complexities. As the number of data points are quite limited per strip, we apply the small sample correction to the AIC (AICc). For models that are generated by least square fitting routines, the AICc is computed in the following way:

$$\mathrm{AICc} = 2k + n \cdot \ln(\mathrm{RSS}) + \frac{2k^2 + 2k}{n - k - 1}. \tag{7}$$

Here k denotes the number of model parameters, n the number of data points and RSS the residual sum of squares. Overall, we fitted exponential profiles; however, we need to account for the radio beam. Therefore, the models that are actually fitted are convolutions of exponential profiles with Gaussian kernels (cf. Dumke et al. 1995). Intrinsic exponential profiles with an intensity, w_0, and a scale height, z_0,

$$w(z) = w_0 \exp\left(\frac{-z}{z_0}\right), \tag{8}$$

---

[6] UGC 5983 is located at 10h52m16.749s +36d35m40.24s (coordinates taken from NASA NED) but does not show radio continuum emission.

[7] In this paper, the energy dependence of the CR diffusion is described as $D(E) = D_0 \cdot (E/\mathrm{GeV})^\mu$.

[8] The energy dependence of the CR diffusion strongly depends on the observed energy range.

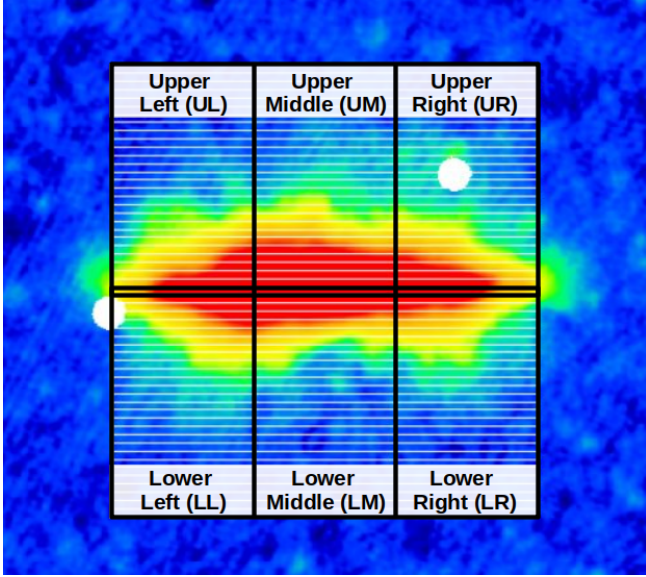[9] https://gitlab.mpifr-bonn.mpg.de/peter/NOD3

Fig. 5. Strip setup on the HBA map of NGC 891. The map has been point-source-subtracted and masked. The six strips (UL, UM, UR, LL, LM, and LR) are indicated with thick black lines. A similar setup is used on all galaxies during box integration with NOD3. Central boxes are part of the lower as well as the upper strips. Left strips have a positive offset, and right strips have a negative one. Individual boxes (thin white lines) have a height of 10″ and a width of 177″ (as listed in Table 5).

need to be convoluted with a Gaussian kernel with a standard deviation, σ,

$$g(z) = \frac{1}{\sqrt{2\pi\sigma^2}}\exp\left(\frac{-z^2}{2\sigma^2}\right), \quad (9)$$

to account for the limited resolution of the images. We tried to fit different profiles, including Gaussian profiles, but the analysed intensity profiles are overall better fitted with exponential functions. We use those fits to get the scale heights used in the following analysis. The most complex model we fit to the vertical profiles is a two-component exponential profile with intensities w_0, w_1 and scale heights z_0, z_1:

$$w_{\text{dual}}(z) = \frac{w_0}{2}\exp\left(\frac{-z^2}{2\sigma^2}\right)\left[\exp\left(\left(\frac{\sigma^2 - zz_0}{\sqrt{2}\sigma z_0}\right)^2\right)\text{erfc}\left(\frac{\sigma^2 - zz_0}{\sqrt{2}\sigma z_0}\right)\right.$$

$$+ \exp\left(\left(\frac{\sigma^2 + zz_0}{\sqrt{2}\sigma z_0}\right)^2\right)\text{erfc}\left(\frac{\sigma^2 + zz_0}{\sqrt{2}\sigma z_0}\right)\right]$$

$$+ \frac{w_1}{2}\exp\left(\frac{-z^2}{2\sigma^2}\right)\left[\exp\left(\left(\frac{\sigma^2 - zz_1}{\sqrt{2}\sigma z_1}\right)^2\right)\text{erfc}\left(\frac{\sigma^2 - zz_1}{\sqrt{2}\sigma z_1}\right)\right.$$

$$\left.+ \exp\left(\left(\frac{\sigma^2 + zz_1}{\sqrt{2}\sigma z_1}\right)^2\right)\text{erfc}\left(\frac{\sigma^2 + zz_1}{\sqrt{2}\sigma z_1}\right)\right]. \quad (10)$$

Here, erfc is the complementary error function. With such a two-component model, one can try to decompose galactic disks and halos. However, such a distinction is not always possible. Furthermore, the intensities w_0 and w_1 as well as the scale heights z_0 and z_1 in the two-component model are degenerate. This can result in very large uncertainties in the model parameters, especially when fitting the model to only a limited number of noisy data points. When the estimated uncertainty of a fitted model

parameter exceeds the parameter value, we reduce the complexity of the model to obtain well-constrained fitting parameters by using a one-component exponential profile:

$$w_{\text{single}}(z) = \frac{w_0}{2}\exp\left(\frac{-z^2}{2\sigma^2}\right)\left[\exp\left(\left(\frac{\sigma^2 - zz_0}{\sqrt{2}\sigma z_0}\right)^2\right)\text{erfc}\left(\frac{\sigma^2 - zz_0}{\sqrt{2}\sigma z_0}\right)\right.$$

$$\left.+ \exp\left(\left(\frac{\sigma^2 + zz_0}{\sqrt{2}\sigma z_0}\right)^2\right)\text{erfc}\left(\frac{\sigma^2 + zz_0}{\sqrt{2}\sigma z_0}\right)\right]. \quad (11)$$

With these models, we can fit radio halo scale heights in each strip. We additionally allow for a shift in the z direction using the following coordinate transformation:

$$z' = z - Z_0. \quad (12)$$

To summarise our scale height fitting process: each strip is fitted with four models: a two-component exponential with shift in the z direction (two), a two-component exponential without shift in z-direction (two_fo), a one-component exponential with shift in the z direction (one), and a one-component exponential without shift in the z direction (one_fo). The model selection is based on the AICc and the model complexity is reduced if the uncertainty of the best-fit parameter exceeds the parameter itself.

6.2. Scale heights

To keep this paper concise, we refer the reader to Appendix B, where we list the fitted model parameters and present the fitted models for each strip. The scale heights averaged per galaxy are listed in Table 6. As an example, we present the fitted profiles of NGC 891 (Fig. 6) and the corresponding fitting parameters (Table 7).

The intensity profile of NGC 891 has already been analysed in the previous works by Mulcahy et al. (2018; MU18) and Schmidt et al. (2019). While Schmidt et al. (2019) analysed a combination of VLA C-band and L-band data, MU18 also analysed the galaxy with help of data from the LOFAR telescope. Both studies extract intensity profiles up to a height of ~3.5 kpc. With the data used in this work, we can follow the intensity profiles much farther into the halo. The newly cleaned CHANG-ES L band allows us to extract accurate intensity profiles up to ~8 kpc for the upper half and to 6 kpc for the lower half of NGC 891. Therefore, we can nearly double the extent of the analysed halo in the L-band data. The improvement in data quality is even more pronounced for the low-frequency dataset. Here, we can follow the intensity profile to a height of ~11 kpc and therefore more than triple the extent of the analysed halo. When averaging over strips where the data allowed two exponential components to be fitted (four out of six strips for HBA), we derive mean scale heights $z_{\text{disk}} = 0.76 \pm 0.25$ kpc and $z_{\text{halo}} = 2.9 \pm 0.5$ kpc for the galactic disk and the halo of NGC 891 in the HBA data. Therefore, the derived scale height of the disk in this work is slightly larger than that derived by MU18 ($z_{\text{disk}} = 0.32 \pm 0.08$ kpc; $z_{\text{halo}} = 2.3 \pm 0.7$ kpc), while the halo scale heights are similar. Both studies correct for the effect of smoothing by the radio beam during the fitting routine. Nevertheless, especially the difference in the measurement of the disk scale height might result from different resolutions (12″ in MU18, 20″ in this work). Due to the larger extent of the strips analysed in this work, the derived halo scale heights might be more reliable compared to previous studies. Judging from the AICc model assessment, none of the L-band data strips shows sufficient complexity to be fit with a two-component model. Averaging over all L-band strips that were fitted with
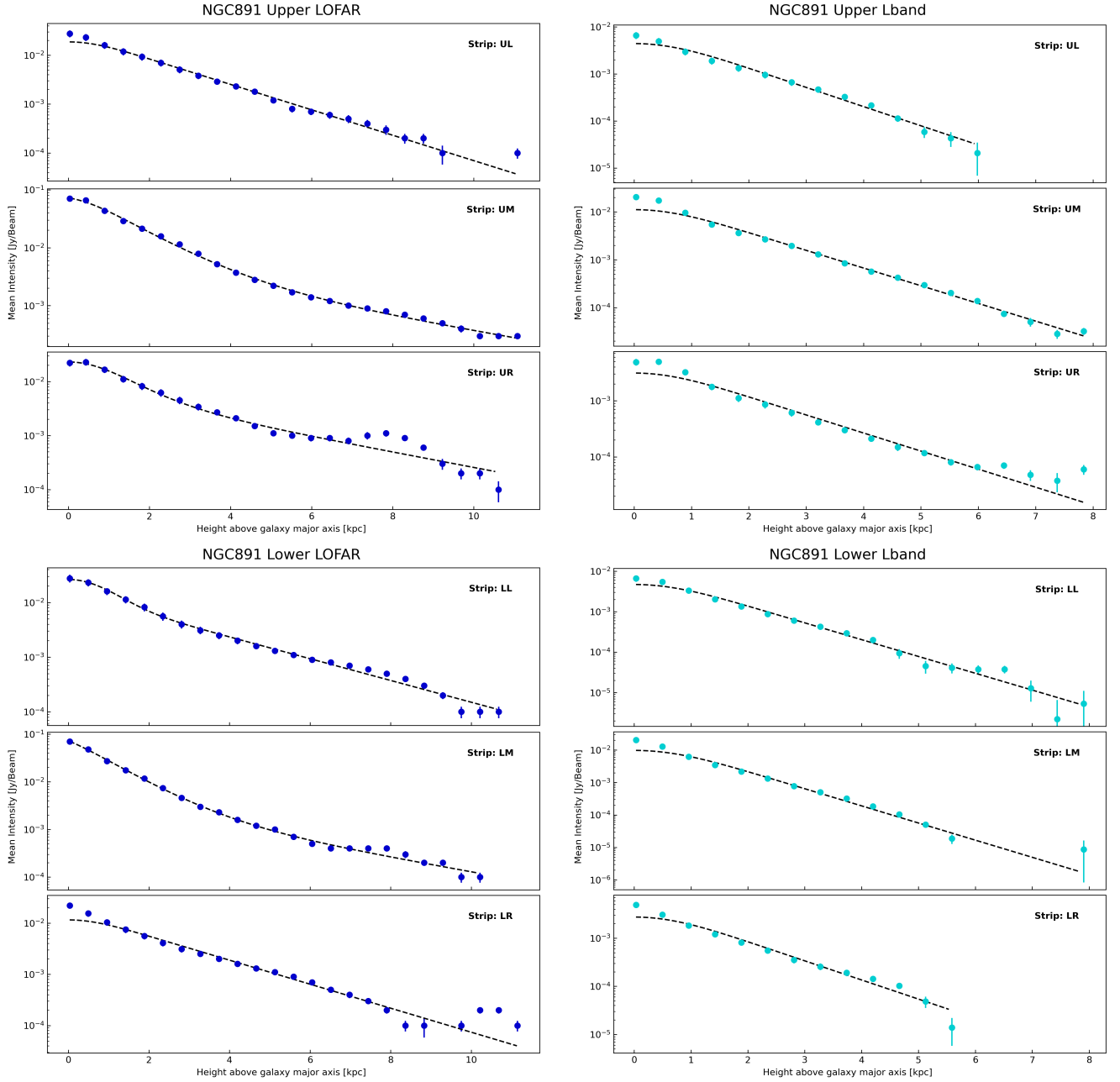
Fig. 6. Vertical radio continuum intensity profiles in the three strips of NGC 891. Left panels show 144-MHz LOFAR data, and right panels show 1.5-GHz JVLA data. Best-fitting double exponential profiles are shown as dashed lines.

one component, we derive a mean scale height of NGC 891 of $z_{1comp} = 1.09 \pm 0.16$ kpc.

Scale heights of NGC 4631 have been analysed before, by Mora-Partiarroyo et al. (2019; MP19) in the 6 GHz and 1.5 GHz bands. With the strips that were fitted with two components in our analysis, we find larger radio halo scale heights than MP19. However, both measurements have fairly large uncertainties ($z_{halo} = 2.1 \pm 0.3$ kpc (this work), $z_{halo} = 1.75 \pm 0.27$ kpc (MP19)). In the HBA data, we report a mean scale height of the galactic halo of $z_{halo} = 4.9 \pm 0.4$ kpc. This is more than double the scale height compared to the higher-frequency data. While MP19 extracted profiles of ~ 6.6 kpc reaching from south to north of the galaxy, we follow the intensity profile $\sim 8-10$ kpc in either direction of the galactic disk, which most probably increases the reliability of our analysis. In the HBA data, the extent of the galactic halo can be analysed on unprecedented

scales. Here, we can follow the intensity profile to a height of 14 kpc[10].

Comparing our results of NGC 4013 to Stein et al. (2019a; ST19) is more difficult than in the case of NGC 891 or NGC 4631, since their profile fitting is based on Gaussian instead of exponential profiles. ST19 report disk (halo) scale heights of 0.36 ± 0.05 kpc (2.0 ± 0.1 kpc) in the VLA L band and 0.47 ± 0.10 kpc (3.1 ± 0.3 kpc) in LOFAR HBA. Our model comparison based on the AICc shows again that the strips are equally well fitted with just a single exponential fit rather than a two-component approach. The radio halo of NGC 4013 will be discussed in more detail in Sect. 8.3.

---

[10] Heald et al. (2022) reached similar extents in their analysis of NGC 5775 but had a lower physical resolution of 2.2 kpc.

Table 6. Fitted radio scale heights per galaxy. One- and two-component model are listed separately.

Band	Two-component			One-component	
	Disk [kpc]	Halo [kpc]	N	Overall [kpc]	N
NGC 891					
L-band	–	–	0	1.09±0.16	6
HBA	0.76±0.25	2.9±0.5	4	1.76±0.09	2
NGC 3432					
L-band	–	–	0	0.86±0.21	6
HBA	–	–	0	0.7±0.4	6
NGC 4013					
L-band	–	–	0	0.60±0.08	6
HBA	–	–	0	0.75±0.14	6
NGC 4157					
L-band	0.7±0.4	1.2±0.2	1	1.16±0.19	5
HBA	1.05±0.16	7±3	2	2.2±0.6	4
NGC 4631					
L-band	0.50±0.08	2.1±0.3	3	1.7±0.5	3
HBA	1.45±0.01	4.9±0.4	2	2.8±0.6	4

Notes. For the two-component models, we distinguish disk and halo scale heights. The Number of stripes (N) that have been fitted with each model is also indicated. If only one stripe has been fitted with a certain model, the uncertainty of the scale heights is computed within χ^2-minimisation. If multiple stripes have been been fitted with a model, the uncertainty is computed via the standard deviation of the sample.

Scale heights of NGC 3432 and NGC 4157 have been fitted with two-component exponential functions in the C band and L band by Krause et al. (2018; L band: NGC 3432: $z_{halo} = 0.92 \pm 0.25$ kpc, NGC 4157: $z_{halo} = 1.08 \pm 0.07$ kpc)[11]. This is in agreement with the values we find, considering the fact that we only fit one-component models for NGC 3432.

Now, we analyse the scale heights of all galaxies as a sample. The model comparison with the AICc shows that most strips can be fitted, with the chosen box integration setup (spatial resolution and box size), with one-component models. For the following analysis we use results from the one-component fits only, since mixing scale heights of one- and two-component models is not advisable at all (also strips that showed enough complexity to be fitted with two components are re-fitted with one-component models for this part of the analysis). In Fig. 7 we compare the radio scale heights of each strip in the L-band and HBA data. In their analysis of 13 galaxies in the L and C band, Krause et al. (2018) report overall similar scale heights in both spectral bands. This picture changes drastically when comparing L-band to HBA profiles. Here, one can see a bi-modality in the data. Galaxies that showed a strong and uniform gradient in the non-thermal SPIX maps (NGC 891, 4157, and 4631) have much larger scale heights in HBA than in the L band and galaxies without such a gradient (NGC 3432) or with a less prominent SPIX gradient (NGC 4013) lie much closer to the one-to-one line. The relative scattering of the individual strips of a galaxy is largest in NGC 4157. Comparing the HBA and L-band contour lines of NGC 4157 in Fig. 3, one can notice that not only the minor axis, but also the major axis is larger in HBA than in the L band. Therefore, the comparison of the box profiles might show

a larger variety. Assuming a rather symmetric galactic magnetic field structure, one interpretation explaining the scatter in the measured scale-height ratios of a given galaxy could also be a space-dependent CR transport mechanism (e.g. space-dependent diffusion coefficient Evoli et al. 2018). In the literature, there are also studies that have observed larger scale heights in the low-frequency data. Mulcahy et al. (2018) report a scale height ratio of 1.7 ± 0.3 for NGC 891 and Heald et al. (2022) find a ratio of 1.2 ± 0.3 in NGC 5775 when comparing L-band and HBA scale heights. We report the mean scale height ratio (average of the ratios of individual strips) for each galaxy in Table 8. These ratios reflect the results from the non-thermal SPIX maps. Those galaxies that show a clear gradient in the SPIX maps also have significantly larger scale heights in HBA than in the L band, as expected.

Following the argumentation of Krause et al. (2018), the observed scale height ratio can predict the dominating CR transport mechanism in the galaxy. First of all, loss-dominated and escape-dominated halos need to be distinguished. In a loss-dominated halo, the synchrotron emission falls below the detection limit because the CREs have lost so much energy through radiation that they can no longer be detected. In escape-dominated halos, the synchrotron radiation drops below the detection limit because of the decreasing number of CREs and lower magnetic field strengths. Of course, the observed expansion of the galaxy halo is actually limited by a combination of both effects, which makes it difficult to argue on the basis of scale heights alone. Nevertheless, for a loss-dominated halo, Krause et al. (2018) report the following frequency dependences on the advection length l_{con} and diffusion length l_{diff} for diffusion with a non-energy-dependent diffusion coefficient D (μ=0), energy-dependent diffusion with $D \propto E^{0.5}$ ($\mu = 0.5$) and advection, which can than be translated into expected scale height ratios r for the frequencies analysed in this paper (144 MHz & 1.5 GHz). We list the derived proportionality and expected ration in Table 9.

We show these relations in Fig. 7 to compare them to the measured scale heights. Most of the scale heights measured in NGC 3432 and NGC 4013 fall even below the energy-dependent diffusion line, while NGC 891 and NGC 4631 seem to be well represented by the $\mu = 0$-diffusion transport. The aforementioned CRE escape process drives the measured scale ratios closer to the one-to-one relation. Because of that, Miskolczi et al. (2019) find in the 1D CR transport modelling that advection models are the best-fitting transport mechanism in NGC 3556, although they find an HBA/L band ratio of 1.8 in the halo, which would point to energy-independent diffusion if only the scale height ratio is considered. Therefore, it seems likely that the halo of NGC 3556 is not loss-dominated.

Heesen et al. (2018b) performed a correlation analysis to find possible relations between the fitted radio scale heights and other measured properties such as SFR, SFR surface density, and the rotation velocity. They did not find a strong correlation between the radio scale height and any of these properties. In Fig. 8, we present the fitted HBA radio scale heights for one- and two-component models separately in comparison to the diameter of the galactic disk, measured on resolution enhanced WISE 22 μm images, and the SFR within the individual strips. In the two-component plots, only the halo scale heights are shown, which show neither a clear trend with the galaxy diameter nor with the SFR.

For the one-component models, one might expect a positive trend for the galaxy diameter as well as the SFR. Therefore, we perform a more detailed correlation analysis where all strips
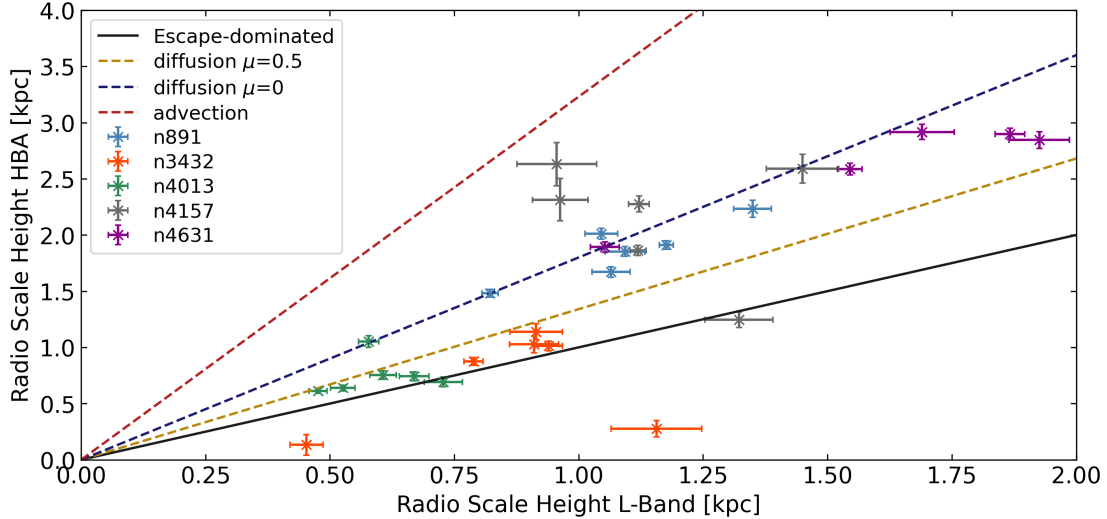
[11] The authors node that their derived disk scale heights are limited in their reliability, because of the resolution of the observations.

Fig. 7. Comparison of fitted non-thermal radio scale heights in the VLA *L* band and LOFAR HBA. For each strip of each galaxy, the radio scale height in the HBA data is plotted against its *L*-band counterpart. Individual galaxies are colour coded as indicated in the legend. The solid black line represents the identity relation one would expect in escape-dominated halos. Dashed lines indicate expected scale height ratios for loss-dominated halos: dark blue represents energy-independent diffusion, gold represents energy-dependent diffusion, and red represents advection.

Table 7. Parameters from box integration model fitting of NGC 891.

v [MHz]	Model	ID	w_0	z_0 [μ Jy beam^{-1}]	w_1 [kpc]	z_1 [μ Jy beam^{-1}]	Z_0 [kpc]	χ_ν^2 [kpc]
1500	one_fo	LR	4.3±0.3	1.09±0.04	–	–	–	2.55
144	one_fo	LR	15.2±1.0	1.85±0.04	–	–	–	4.02
1500	one_fo	UR	4.5±0.3	1.35±0.04	–	–	–	3.50
144	two_fo	UR	32±5	0.77±0.15	6.7±1.4	3.04±0.26	–	3.41
1500	one_fo	LM	17.2±0.8	0.822±0.016	–	–	–	7.41
144	two	LM	188±113	0.87±0.08	5.8±2.1	2.9±0.4	−1.0±0.7	1.01
1500	one_fo	UM	16.9±0.6	1.176±0.014	–	–	–	5.88
144	two	UM	111±18	1.05±0.10	6.6±2.3	3.6±0.5	−0.33±0.27	0.50
1500	one_fo	LL	7.4±0.6	1.05±0.03	–	–	–	1.21
144	two_fo	LL	43±22	0.37±0.21	13.9±1.6	2.18±0.08	–	1.22
1500	one_fo	UL	6.9±0.6	1.07±0.04	–	–	–	1.05
144	one_fo	UL	25.4±1.9	1.67±0.05	–	–	–	1.05

Notes. Frequency of fitted data, model identifier, strip identifier, peak intensity and scale height of the first exponential component, peak intensity and scale height of the second exponential component (if applicable), offset in the *z* direction (if applicable), and reduced χ-square. The corresponding profiles are shown in Fig. 6. A complete list of all galaxies can be found in Table B.1.

Table 8. One-component radio scale height ratios of HBA and *L*-band profiles.

Galaxy	HBA/*L*-band ratio	SPIX-gradient
NGC 891	1.71±0.12	Strong, uniform
NGC 3432	0.8±0.4	No/disordered
NGC 4013	1.27±0.27	Less prominent
NGC 4157	1.9±0.6	Strong, uniform
NGC 4631	1.65±0.11	Strong, uniform

Notes. Uncertainties represent the spread of the different strips of a galaxy.

Table 9. Derived proportionalities of the diffusion lengths and advection lengths and the observed radio frequency dependencies (as derived by Krause et al. 2018) as well as the expected scale height ratios for the HBA and the *L* band.

Transport	Proportionality	Ratio
Loss-dominated:		
Diffusion ($\mu = 0$)	$l_{\mathrm{diff}} \propto \nu^{-1/4}$	1.80
Diffusion ($\mu = 0.5$)	$l_{\mathrm{diff}} \propto \nu^{-1/8}$	1.34
Advection	$l_{\mathrm{con}} \propto \nu^{-1/2}$	3.23
Escape-dominated:		
Advection	$l_{\mathrm{con}} = $ const.	1.00

have been fitted with one-component models in Fig. 9. Obviously there is a strong link between the HBA radio scale height, *L*-band scale height and the HBA/*L* band ratio (*r*). However, here we are more interested in a link of the radio measurements

of the halo with other quantities such as SFR or the magnetic field. The diameter of the galactic disk seems to be a quite good predictor for the measured HBA scale height (Spearman-r: 0.67,
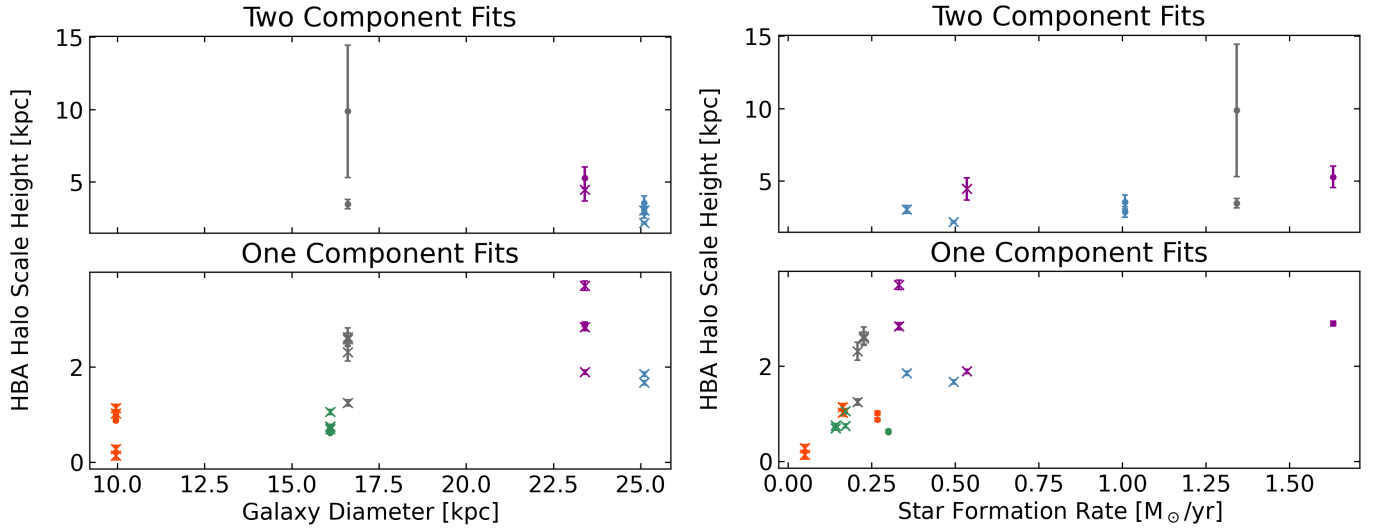
Fig. 8. Individual radio halo scale heights plotted against galaxy diameter (left) and star formation within the individual strip (right). Two-component and one-component fits are displayed separately. In the plots of the two-component fits, only the halo scale heights are shown. Dots represent the central strips and *x* symbols the outer strips of each galaxy. NGC 891 is shown in blue; NGC 3432 in orange; NGC 4013 in green; NGC 4157 in grey; and NGC 4631 in magenta (same as Fig. 7).

p-value: 5e–5)[12] The SFR is equally strongly linked to z_0; however, the scatter plot does show outlier values with much larger SFRs than the average trend. We also checked if the specific star formation rate (sSFR; based on the mass estimates in Table 1) is a better predictor but the sSFR does not perform better than the SFR. Therefore, we just present the SFR values in Fig. 9. We do not find significant correlations between z_0 and the SFR surface density nor the magnetic field strength. Overall, the *L*-band scale height (and therefore also the ratio *r*) is less strongly linked to the diameter and SFR compared to the HBA scale height.

The strongest correlations we find in this study are (a) the link between the equipartition magnetic field strength and the SFR in the individual strips, and (b) between the SFR surface density and the gravitational potential. A correlation between the SFR and the magnetic field strength has already been reported in studies of dwarf galaxies (Chyży et al. 2011), the KINGFISHER nearby galaxy sample (Tabatabaei et al. 2017), and nearby edge-on galaxies (Heesen et al. 2018b). However, the relation found in this study is most probably affected by the study setup. Meaning that we simply measure higher SFRs and magnetic field strengths in the centre of a galaxy, because of the radial dependence and not only because of a link between the SFR and the galactic magnetic field. The same is also most likely true for the link between the SFR surface density and the gravitational pull.

Concluding this section, we find that even the predictors that were found to be best in this study – measured SFR within a strip and the galaxy diameter – are not suited to reliably constrain the radio halo size. The formation of a galactic wind seems to be too complex to be predicted by a single parameter in such a small sample. We continue the analysis of galactic winds driven by stellar feedback by fitting the extracted intensity profiles with a 1D CR-transport model.

---

[12] It is important to note that the *p*-value for such small samples is not completely reliable. However, the measured correlation coefficients are large enough to be reliable and the trends are also visible in the scatter plots.

7. Stellar-feedback-driven winds

In this section we extend the analysis of the extracted profiles in order to derive physical parameters of the galactic wind. The section is structured as follows: First, we introduce the models that are used to analyse the CR transport mechanisms in the galaxies and the input and output parameters for each galaxy. Further, we motivate the model choice for each galaxy and explain the exclusion of NGC 3432 from the further analysis. In Sect. 7.2 the results of the diffusion model fitting of NGC 4013 are displayed. In the last subsection (Sect. 7.3), we present the results of the completed advection model fitting for NGC 891, NGC 4157, and NGC 4631.

7.1. Cosmic ray transport models

The 1D CR transport modelling is performed with the SPectral INdex Numeral Analysis of K(c)osmic-ray Electron Radio-emission (SPINNAKER) code (Heesen et al. 2016, 2018b). SPINNAKER fits vertical intensity profiles of multiple frequencies and the resulting SPIX profiles to several wind models (diffusion or advection). The latest SPINNAKER extension for advection-dominated galactic winds, the so called flux tube model, has been published by Heald et al. (2022). In the literature, several studies already made use of synchrotron radiation to analyse the CR transport of nearby edge-on galaxies (cf. Schmidt et al. 2019; Miskolczi et al. 2019; Stein et al. 2019a). Some of those studies analysed galaxies that are also part of the present work. However, as pointed out by Heald et al. (2022), the new flux tube model has several benefits compared to the previous approaches (e.g. magnetic and velocity scale heights are fitted simultaneously in the flux tube model, whereas they had to be fitted separately before). Therefore, we apply the advection flux tube model (accounting for advection losses) introduced by Heald et al. (2022). The model assumes an hyperboloidal tuneable flux tube, an isothermal wind, and exponentially declining gravitational acceleration for increasing heights above the galactic disk. Therefore, the cross sectional area *A* of the flux tube above the disk is described as
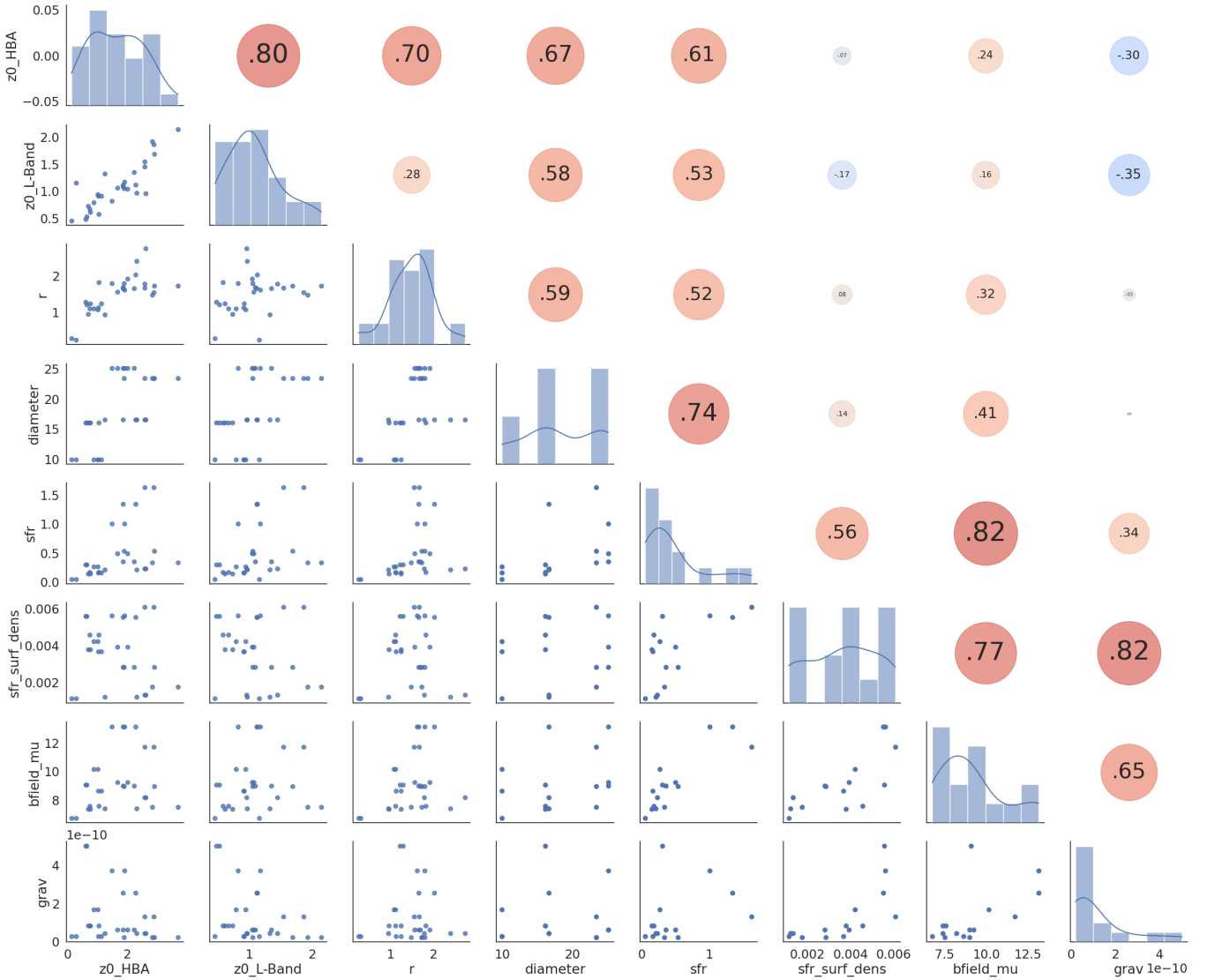
Fig. 9. Correlation analysis of several physical properties in comparison to the fitted HBA and *L*-band radio scale heights ($z_{0, \text{HBA}}$, $z_{0, L\text{-band}}$) and the ratio of HBA and the *L* band (r). The main diagonal displays the distribution of z0 and *r* as well as the other analysed quantities (SFR, SFR surface density, and equipartition magnetic field strength) as histograms and kernel density estimates. Bottom: bivariate scatter plots for pairs of the analysed quantities with interpolation line. Top: colour coded (blue: negative, red: positive) Spearman rank correlation coefficients.

$$A(z) = A_0 \left[1 + \left(\frac{z}{z_0} \right)^\beta \right]. \tag{13}$$

The model results in a hyperboloid if the free parameter β is set to $\beta = 0$. Further, Heald et al. (2022) assume a magnetic field that declines with the midplane flow radius, r, and the advection speed, v:

$$B(r, v) = B_0 \left(\frac{r}{r_0} \right)^{-1} \left(\frac{v}{v_0} \right)^{-1}. \tag{14}$$

Here, B_0 [µG] describes the magnetic field strength in the galactic plane. For further details about the model, we refer to Heald et al. (2022, Sect. 4.3 and Appendix A). To describe the hyperboloidal flux tube, we introduce the base radius of the flux tube, R_0, its scale height, z_0, and the power law index that describes its opening angle, β. With this model, we fit the vertical height, z_c, of the critical point, the wind speed at the critical point, v_c, and the power law index of the CRE injection spectrum, γ. The critical point denotes the transition of a subsonic to a supersonic galactic wind. As input parameters, we provide the $z = 0$ radius of

the flux tube R_0 (in this work defined as the strip width of each galaxy), rotational velocities, and the magnetic field strength B_0 within the galactic disk. B_0 is determined as the average magnetic field strength for each strip measured on equipartition magnetic field maps, published in Heesen et al. (2022a) in 20″ wide boxes (see Table 5 for physical extents). Heesen et al. (2022a) use the revised equipartition formula of Beck & Krause (2005) to compile their magnetic field strength maps. In order to derive magnetic field strength values from radio continuum data, some assumptions have to be made. First of all, one assumes equipartition between the CRs and the total magnetic energy, which is similar to a minimisation of the total energy density. Another important value that needs to be estimated to predict the magnetic field strength via the equipartition approach, is the proton-electron ratio K_0. Heesen et al. (2022a) use $K_0 = 100$. The applied value of the proton-electron ratio bases on measurements in our Galaxy (Cummings et al. 2016). We fit for optimal solutions by incorporating a grid-search algorithm implemented in the interactive extension of SPINNAKER, SPINTERACTIVE (Miskolczi et al. 2019).

Table 10. Output parameters from SPINNAKER advection-model fitting.

Stripe	z_{max} [kpc]	γ	v_c [km s^{-1}]	z_0 [kpc]	β	z_c [kpc]	χ^2_ν
			NGC 891				
LR	5.2	$2.40^{+0.08}_{-0.06}$	128^{+18}_{-8}	$3.9^{+0.5}_{-0.7}$	$1.53^{+0.04}_{-0.1}$	$1.0^{+0.6}_{-0.6}$	3.1
LM	5.2	$2.16^{+0.07}_{-0.05}$	152^{+24}_{-11}	$2.4^{+0.2}_{-0.3}$	$1.73^{+0.05}_{-0.08}$	$0.2^{+0.1}_{-0.1}$	3.4
LL	5.2	$2.20^{+0.08}_{-0.07}$	129^{+8}_{-6}	$4.9^{+0.6}_{-0.6}$	$1.85^{+0.02}_{-0.05}$	$2.3^{+0.9}_{-0.7}$	3.6
UR	6.0	$2.32^{+0.13}_{-0.07}$	167^{+38}_{-14}	$5^{+0.7}_{-0.9}$	$1.79^{+0.13}_{-0.18}$	$1.1^{+0.6}_{-0.6}$	2.2
UM	7.8	$2.11^{+0.08}_{-0.05}$	189^{+26}_{-16}	$3.55^{+0.3}_{-0.4}$	$1.78^{+0.06}_{-0.07}$	$0.34^{+0.12}_{-0.13}$	3.4
UL	6.0	$2.27^{+0.08}_{-0.08}$	137^{+9}_{-8}	$5.0^{+0.8}_{-0.5}$	$1.85^{+0.03}_{-0.04}$	$2.0^{+0.9}_{-0.5}$	3.6
			NGC 3432				
LM	3.9	$2.13^{+0.09}_{-0.16}$	240^{+420}_{-135}	$3.0^{+0.4}_{-0.2}$	$2.10^{+0.30}_{-0.35}$	<0.9	1.5
UM	3.8	$2.17^{+0.12}_{-0.12}$	233^{+760}_{-100}	$2.7^{+0.2}_{-0.4}$	$2.2^{+0.20}_{-0.4}$	<0.9	0.55
			NGC 4013				
LR	3.6	$2.4^{+0.2}_{-0.2}$	122^{+85}_{-26}	$2.5^{+0.4}_{-0.3}$	2.0	$0.9^{+0.9}_{-0.6}$	0.4
LM	2.9	$2.30^{+0.08}_{-0.04}$	100^{+55}_{-14}	$1.1^{+0.1}_{-0.1}$	1.6	<1.4	1.7
LL	3.6	$2.25^{+0.15}_{-0.10}$	180^{+610}_{-60}	$2.1^{+0.4}_{-0.3}$	2.0	<1.4	1
			NGC 4157				
LM	7.2	$2.21^{+0.09}_{-0.06}$	177^{+24}_{-12}	$4.7^{+0.4}_{-0.7}$	$1.72^{+0.04}_{-0.10}$	$0.4^{+0.1}_{-0.2}$	1.7
LL	6.0	$2.39^{+0.09}_{-0.10}$	128^{+6}_{-5}	$8.2^{+0.8}_{-1.1}$	$2.21^{+0.02}_{-0.02}$	$4.7^{+1.0}_{-1.2}$	0.5
UM	7.1	$2.26^{+0.08}_{-0.08}$	226^{+26}_{-24}	$5.3^{+0.4}_{-0.5}$	$2.05^{+0.14}_{-0.12}$	$0.6^{+0.2}_{-0.2}$	2.81
UL	4.7	$2.34^{+0.10}_{-0.08}$	164^{+10}_{-8}	$13.0^{+2.0}_{-2.5}$	$2.66^{+0.02}_{-0.04}$	$7.0^{+0.5}_{-2.0}$	2.9
			NGC 4631				
LR	6.0	$2.2^{+0.16}_{-0.20}$	95^{+12}_{-12}	$7.3^{+1.7}_{-2.1}$	$1.80^{+0.10}_{-0.14}$	$3.1^{+3.2}_{-2.0}$	0.58
LM	5.3	$2.1^{+0.10}_{-0.04}$	95^{+20}_{-10}	$3.1^{+0.5}_{-0.7}$	$1.20^{+0.08}_{-0.08}$	<0.72	1.0
LL	6.0	$2.3^{+0.30}_{-0.26}$	150^{+55}_{-26}	13^{+7}_{-4}	$2.80^{+0.10}_{-1.30}$	$4.9^{+0.9}_{-4.3}$	0.33
UR	7.9	$2.45^{+0.24}_{-0.09}$	115^{+114}_{-22}	$4.7^{+1.0}_{-2.3}$	$1.30^{+0.15}_{-0.36}$	<0.72	1.9
UM	10.5	$2.20^{+0.14}_{-0.05}$	145^{+34}_{-15}	$3.7^{+0.4}_{-1.0}$	$1.25^{+0.10}_{-0.10}$	<0.72	3.0
UL	10.1	$2.45^{+0.28}_{-0.12}$	125^{+40}_{-15}	$9.4^{+3.2}_{-3.1}$	$1.25^{+0.12}_{-0.14}$	$0.5^{+3.2}_{-0.5}$	0.5

Notes. The maximal height of the fitting region, z_{max}; power law index of the CR injection spectrum, γ; wind speed at the critical point, v_c; scale height of the flux tube, z_0; power law index of the flux tube, β; height of the critical point, z_c; reduced chi square of the best-fitting model, χ^2_ν, computed as the quadratic mean of the two intensity profiles and the SPIX profile.

As shown by ST19, the CR transport of NGC 4013 is most probably dominated by diffusion. Therefore, we rechecked for all strips of NGC 4013 if the diffusion model (as described in Heesen et al. 2019 and Stein et al. 2019a) still fits the data better, compared to the newly developed flux tube advection model. Here, we only consider energy-independent ($\mu = 0$) diffusion[13]. All other galaxies (NGC 891, NGC 3432, NGC 4157, and NGC 4631) are only fitted with the flux tube advection model from Heald et al. (2022).

Input parameters for the galaxies can be found in Table 1 (v_{rot}) and Table 5 (B_0, R_0, beam resolution). The resulting output parameters of the individual strips for all SPINNAKER advection fits are listed in Table 10 and the results from the diffusion fits are summarised in Table 11. As an example, in Fig. 10

Table 11. Output parameters from SPINNAKER energy-independent diffusion-model fitting.

Strip	z_{max} [kpc]	γ	D_0 [cm^2 s^{-1}] $\times 10^{28}$	h_z [kpc]	χ^2_ν
			NGC 4013		
UR	3.5	$2.30^{+0.2}_{-0.1}$	8^{+30}_{-5}	$1.40^{+0.1}_{-0.2}$	1.0
UM	3.5	$2.20^{+0.2}_{-0.1}$	$1.4^{+2.8}_{-0.7}$	$1.20^{+0.1}_{-0.1}$	1.0
UL	3.5	$2.20^{+0.2}_{-0.1}$	$1.4^{+2.8}_{-0.7}$	$1.20^{+0.1}_{-0.1}$	1.0

Notes. The maximal height of the fitting region, z_{max}; power law index of the CR injection spectrum, γ; energy-independent diffusion coefficient, D_0; exponential scale height of the magnetic field, h_z; reduced chi square of the best-fitting model, χ^2_ν, computed as the quadratic mean of the two intensity profiles and the SPIX profile.

---

[13] We note that energy-independent diffusion refers to the CR energy range that is probed with radio synchrotron observations (hundreds of MeV to a few GeV). Energy-independent diffusion has found to be a good fitting model for CR transport probed with data that is similar to ours in M 51 (Dörner et al. 2023). For higher energies, the CR diffusion coefficient is expected to be energy dependent.

we show best-fitting models for one strip each of NGC 891, NGC 4013, and NGC 4631. All other SPINNAKER fits are

displayed in Appendix C. To summarise the SPINNAKER-fitting results, we report that all strips of NGC 891 and NGC 4631 have been successfully fitted with the flux tube advection model. For NGC 4157, we fitted four strips with the advection model and excluded the upper and lower right strips from the further analysis as the resulting SPIX profiles did not allow a proper fitting of the model. As expected from the SPIX map of NGC 3432, we do not find a clear gradient in the SPIX profiles of this galaxy (which is a needed requirement for every CR-propagation process). Nonetheless, to be consistent we present to best-fitting advection model (for the two middle strips), but the wind velocity is basically unconstrained. We therefore exclude NGC 3432 from further analysis, as its interaction with UGC 5983 has most likely disrupted its radio halo.

7.2. Cosmic ray diffusion

NGC 4013 shows mixed results. We find that the upper half of the halo fits better with the energy-independent diffusion model while the lower halo seems to be dominated by advection. Due to the limited extend of the halo, each profile of NGC 4013 is sampled with only five data points (see the middle panel of Fig. 10). Therefore, we reduce the complexity of the advection model by excluding β from the fitting process. Only two of the three strips (UM and UL) of NGC 4013 that have been fitted with a diffusion model, result in a reasonably constrained diffusion coefficient D_0.

7.3. Cosmic ray advection

For the galaxies that have been overall successfully fitted with the advection flux tube model (NGC 891, NGC 4157, and NGC 4631), we present the velocity and magnetic field profiles in Fig. 11. In the left column of Fig. 11, we show the fitted wind velocities. First of all, we note that although the SPINNAKER wind profiles start at an altitude of $z = 0$ kpc, the motions within the galactic disk are predominantly turbulent. From there on, the wind starts to evolve and will eventually start to dominate the overall motion. Therefore, we indicate the extent of the galactic disk, approximated from the disk component scale height of the fitted two-component models in each galaxy. At some point within this range, we expect the wind to form and dominate over turbulent motions. Since the wind solutions studied in this paper are accelerated winds, the wind material in this context will eventually leave the gravitational potential. However, in order to better understand the variety of CR-driven winds, we compare the wind velocities to the escape velocity of a spherical, truncated iso-thermal dark matter halo with a assumed size of $R_{\max} = 30$ kpc[14]. Following Veilleux et al. (2005) and Miskolczi et al. (2019), the escape velocity, $v_{\rm esc}$, at radius r can be computed for known rotation velocities, $v_{\rm rot}$:

$$v_{\rm esc}(r) = \sqrt{2} \cdot v_{\rm rot} \sqrt{1 + \ln\left(\frac{R_{\max}}{r}\right)}. \tag{15}$$

The escape velocities for the middle strip of each galaxy is shown in black in Fig. 11, for comparison. Overall, we find that the wind velocities of the central strips are higher than in outer strips. For NGC 4157, the split between inner and outer strips is very distinct. Here, the wind in the upper middle strip reaches

---

[14] We note that dark matter halo shapes and profiles have shown to be more complex and that the expected halo size strongly depends on the galaxy environment. However, we chose this simplified assumption to be comparable to previous studies. For more details about halo sizes we refer to e.g. Prada et al. (2003), Limousin et al. (2007), and Somerville et al. (2018).
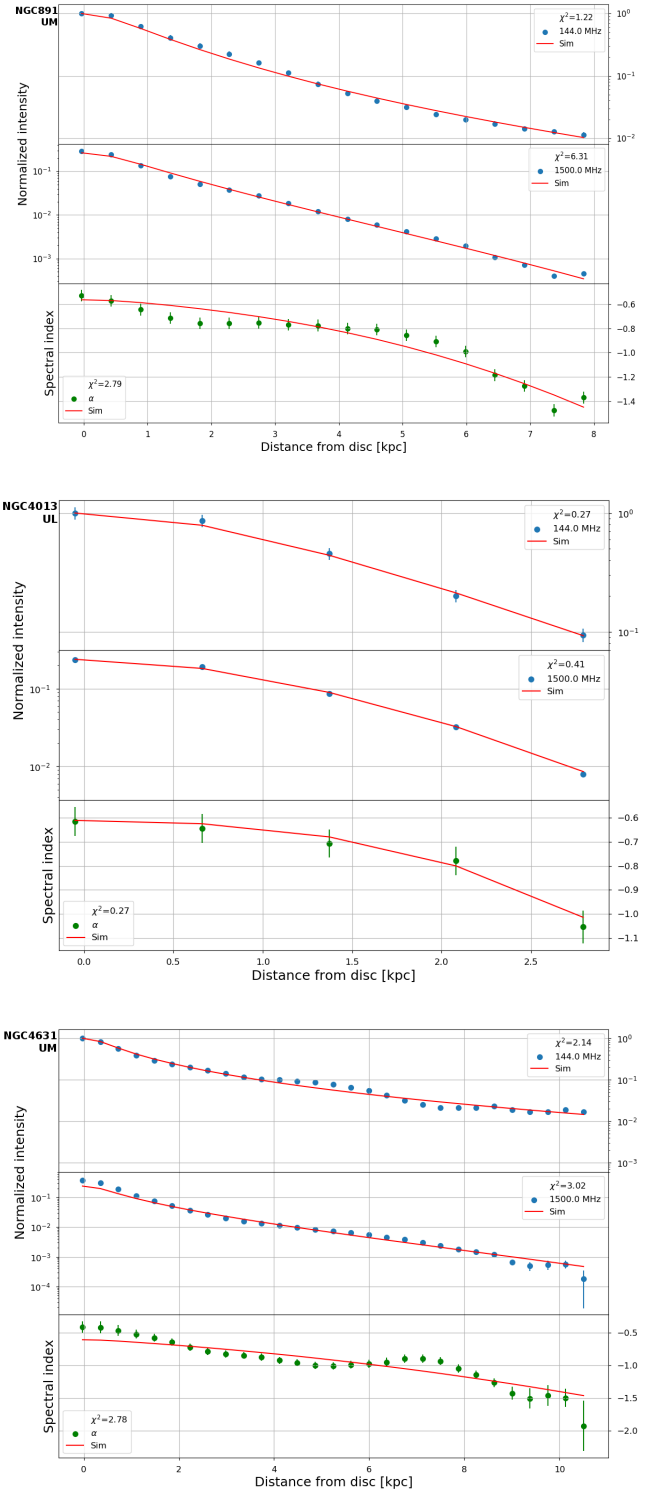

Fig. 10. Best-fitting profiles for NGC 891 UM (top panel), NGC 4013 UL (middle panel), and NGC 4631 UM (bottom panel). For each galaxy, SPINNAKER fits the LOFAR HBA (top graph) and L-band (middle graph) intensity profiles as well as the SPIX profile (bottom graph) simultaneously. The model is shown as a red line. The advection model is applied to NGC 891 and NGC 4631, while the presented strip of NGC 4013 is fitted with a diffusion model.

the escape velocity at 6 kpc. The spread of the velocity profiles of NGC 891 is much smaller compared to NGC 4157 and the wind does not reach the escape velocity within the first 8 kpc of its path. As the rotation velocity of NGC 4631 is much slower
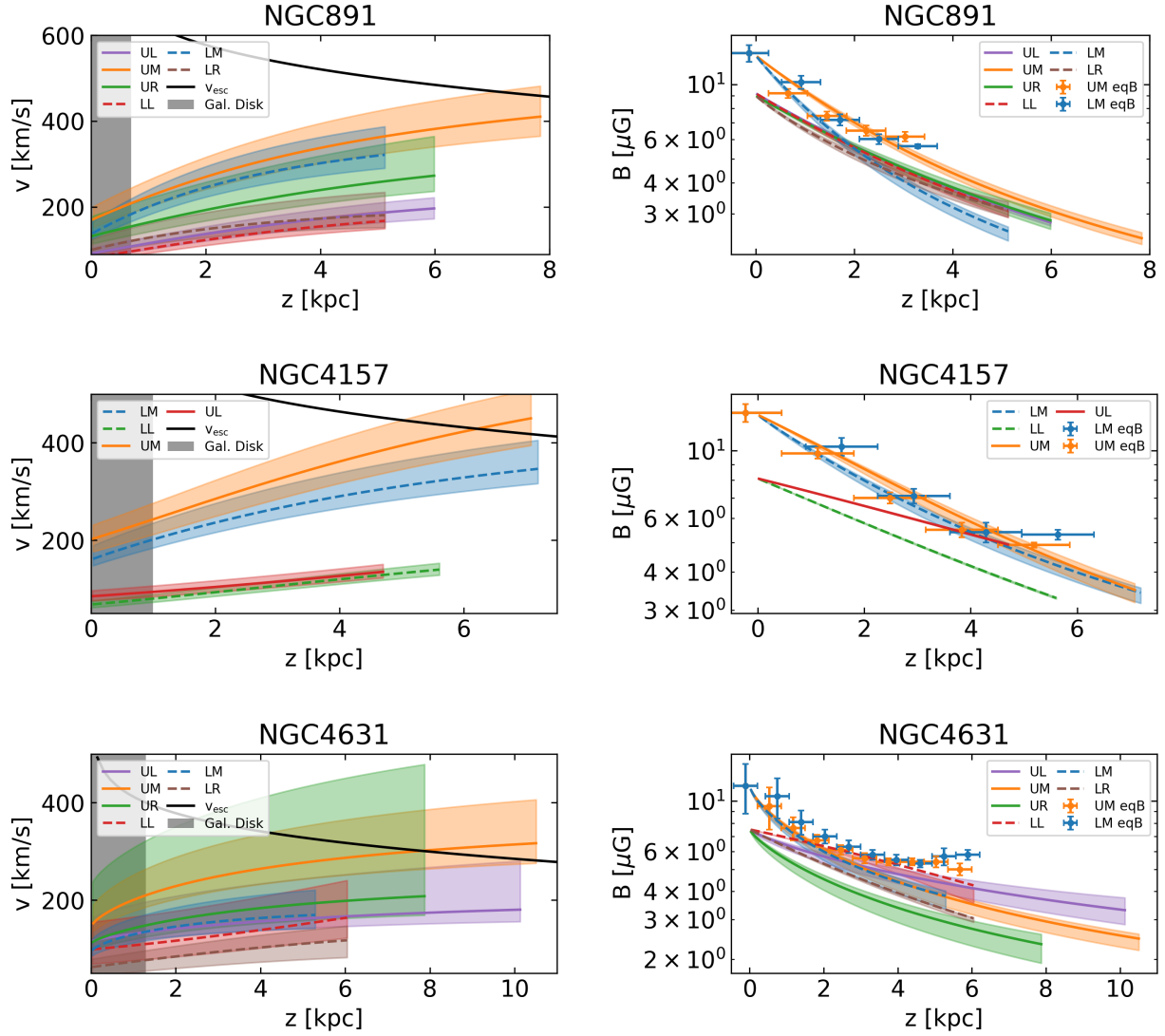
Fig. 11. Velocity (left) and magnetic field (right) profiles for all fitted strips of a galaxy. From top to bottom panel: NGC 891, NGC 4157, NGC 4631. The extent of the galactic disk (estimated via the scale height of the HBA disk components (Table 6) is indicated with a black bar in the velocity profile plots. Dashed lines represent strips pointing downward, solid lines represent upward strips. Lines are best-fitting models and shaded areas indicate one-σ uncertainties. Escape velocities are computed for the central strip of each galaxy via Eq. (15), assuming a truncated dark matter halo size of 30 kpc.

compared to NGC 891 and NGC 4157, the computed escape velocity is also lower. Therefore, the galactic wind of NGC 4631 reaches escape velocity in the UM strip at 8 kpc.

The right column of Fig. 11 displays the magnetic field strength models for the fitted strips. In addition, we compare these profiles to the magnetic field strength measured on the equipartition maps published by Heesen et al. (2022a). Here, we can only present equipartition profiles for the central strips as the extent of the maps is not large enough to also properly sample the outer strips. We find good agreement between the equipartition and the modelled magnetic field strength profiles. In the case of NGC 4157 and NGC 4631, one might suspect a flattening of the equipartition profile around a value of approximately 4 μG but deeper datasets would be needed to confirm such a conjecture.

8. Discussion

In the following, we discuss our results of the non-thermal SPIX analysis regarding the influence of thermal absorption, the sub-

structure that was found in the intensity and SPIX profiles, the CR transport of NGC 4013 in particular, as well as the results of the advection flux tube modelling, and we compare our findings to relevant previous works.

8.1. Non-thermal spectral index

For the observed frequencies, the power-law index of the CRE injection spectrum is expected to be $\gamma_{\rm inj} \approx -2.2$, which translates to an observed radio SPIX of $\alpha_{\rm inj} \approx -0.6$ (Heesen 2021). In the sample we studied, the observed spectral indices within the galactic disks are flatter than the expected value, with NGC 4631 being the most extreme example. Here, a region within the galactic disk (slightly to the left of the galaxy centre) has a non-thermal SPIX of $\alpha_{\rm nth} = -0.4$. In the following, we call this area the region of interest (ROI). We consider two possible rationales for this finding. First of all, the thermal emission within the star-forming regions in the galactic disk might have been underestimated. This would lead to a higher flux density in the L-band measurement and therefore to a flatter SPIX. However, to change

the measured SPIX from −0.4 to −0.6, the thermal contamination of the synchrotron emission in the *L* band would still have to be of the order of 40% after thermal correction, which seems very unlikely considering that this is the maximum total fraction of thermal emission found in the sample.

The second mechanism to consider is thermal absorption in the low-frequency measurement. Due to thermal absorption, the low-frequency pure synchrotron flux density measurement would be underestimated and result in a flatter SPIX. Based on measurements within our Galaxy, Orlando & Strong (2013) predict the peak of the synchrotron spectrum for the inner Galaxy to be at approximately 100 MHz, considering that the ROI is the region with high SFR, the synchrotron peak will at higher frequencies, which makes a influence of thermal absorption on the low frequency probable. Whether our measurements are affected by thermal absorption can be checked by comparing our SPIX map to the findings of MP19 and Vijayan et al. (2022). MP19 show a non-thermal SPIX map based on VLA 1.6 GHz (*L*-band) and 6 GHz (*C*-band) data and Vijayan et al. (2022) present a SPIX map based on 315 MHz and 745 MHz data from the upgraded Giant Metrewave Radio Telescope (uGMRT)[15]. For clarity, we summarise the non-thermal SPIX values for the ROI (read from the published SPIX maps) of MP19, our study and Vijayan et al. (2022) here:

– MP19 (1.5 GHz and 6 GHz):
  $\alpha_{\rm nth} = -0.6$ (expected value for freshly injected CREs).
– Our study (144 MHz and 1.5 GHz):
  $\alpha_{\rm nth} = -0.4$.
– Vijayan et al. (2022; 315 MHz and 745 MHz):
  $-0.2 < \alpha_{\rm nth} < -0.4$.

The MP19 finding allows us to conclude that the *L*-band data are not affected by thermal absorption. As the SPIX for the ROI read from the uGMRT-SPIX map is even flatter than the SPIX value from our analysis, one can suspect that the peak of the synchrotron spectrum for the high star formation regions lies between 315 MHz and 745 Mhz, which is the reason for the flat SPIX measurement. We further underline our findings in Fig. 12. Here, we fit the emission measure (EM) of the region, as described in Adebahr et al. (2013, Eq. (11)). In the fit we include an opacity, τ, that adds an absorption term to the assumed power law of the pure synchrotron emission:

$$S = S_0 \left(\frac{\nu}{\nu_0}\right)^{\alpha} e^{-\tau}. \tag{16}$$

Following Wills et al. (1997) and Adebahr et al. (2013), for free-free absorption, the absorption coefficient is given by

$$\tau = \frac{8.2 \times 10^{-2} \nu^{-2.1} \rm EM}{T_e^{1.35}}. \tag{17}$$

Under these assumptions, the peak of the synchrotron spectrum is at ~200 MHz. For this region, the best-fitting EM is ~3.9 × 10^5 pc cm^{-6}, which is comparable to the EM in the core region of M 82 of ~3.2 × 10^5 pc cm^{-6} (Adebahr et al. 2013).

Another possible way to explain the hardening of the observed CR spectrum are re-acceleration processes as described by Thornbury & Drury (2014), Lerche & Schlickeiser (1980, 1982). Lerche & Schlickeiser (1980) conclude that re-acceleration processes can change the SPIX between low and high-frequency radio data by $\Delta\alpha \leq 0.5$.

---

[15] As they use 315 MHz and 745 MHz data, the influence of thermal emission can be ruled out.
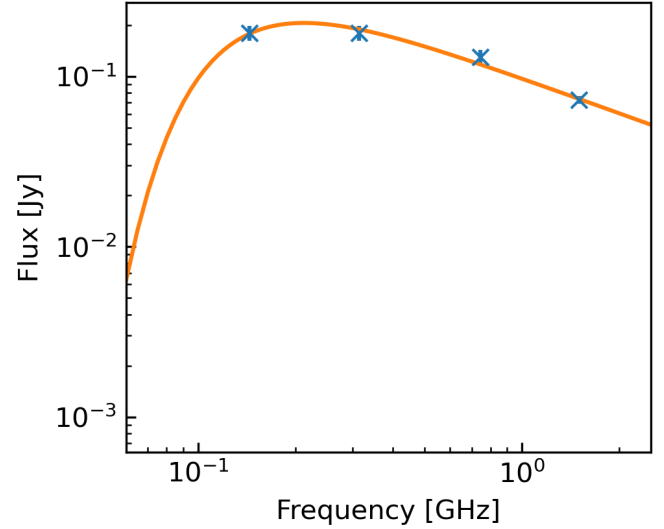

Fig. 12. Double logarithmic diagram displaying the flux measurements of the region with a very flat SPIX in NGC 4631 at the following frequencies: LOFAR HBA (144 MHz), uGMRT (315 MHz and 745 MHz; data taken from Vijayan et al. 2022), and VLA *L* band (1.5 GHz). The orange line displays the synchrotron spectrum, while accounting for thermal absorption with the best-fitting EM.

Overall, we find thermal absorption to be the more likely process to explain the flat SPIX values in this region. Although (Basu et al. 2015) conclude that thermal absorption has no significant influence on integrated low-frequency radio measurements of star-forming galaxies, they nevertheless suggest that it may play a role in compact regions close to the galaxy centre. Furthermore, Very Long Baseline Interferometry (VLBI) measurements of the nuclear starburst of M 82 also show that, for compact regions, thermal absorption influences the low-frequency radio data (Wills et al. 1997; Varenius et al. 2015). We therefore deduce that the LOFAR measurements, within the galactic disk, might be affected by thermal absorption. In order to check if our scale height or CR transport analysis is affected by this phenomenon, we reran the scale height- and SPINNAKER-fitting by removing the $z = 0$ flux measurement, but the results did not change significantly. We therefore do not expect thermal absorption to have a strong influence on our analysis of the radio halo.

8.2. Substructure in intensity and non-thermal spectral index profiles

The analysis of the box integration profiles shows that the intensity profiles are preferably fitted with one- or two-component exponential profiles rather than with Gaussian profiles. Still, for some strips of NGC 891 and NGC 4631, the box integration reveals a significant substructure that is imprinted onto the intensity profiles. Pakmor et al. (2017) find in their analysis of 30 high-resolution cosmological zoom simulations of Milky Way-like galaxies that the vertical magnetic field strength profiles in the inner and outer parts of the galaxy each follow different exponential profiles. They report that the break of the profiles typically occur at a height of 5−15 kpc. Such a break in the magnetic field strength will certainly affect the observed synchrotron profile, which could be at least part of an explanation for the observed substructure. However, the substructure seems to be more complex than a single break in the magnetic field strength

profile could explain. For the UR strip of NGC 891 (see the top-left panel of Fig. 6), this deviation is most probably caused by the residual of an incompletely subtracted background or foreground source. The substructures imprinted on the profiles of NGC 4631 do not seem to result from point source residuals. A careful manual inspection of the total power image did not reveal any background sources.

The observed substructure of the intensity profiles propagates directly into the observed SPIX profiles. We find plateaus in the SPIX profiles (e.g. Fig. 10, top panel: NGC 891 UM) as well as an actual increase of the SPIX values (e.g. Fig. 10, bottom panel: NGC 4631 UM). While NGC 891 and NGC 4631 show a lot of substructure in their intensity and SPIX profiles (see Appendix C), the fitted profiles of NGC 3432, NGC 4013, and NGC 4157 follow the predicted SPINNAKER models without major deviations. A flattening or an actual increase of the SPIX profile points to a rejuvenation process of the CREs, meaning that there needs to be a process that allows the CREs to lose less energy, or even gain energy. Currently, there is no model implemented in SPINNAKER that accounts for such a rejuvenation of CREs. In the ideal magneto-hydrodynamic simulations of a rotating Milky Way-type disk galaxy of Vijayan et al. (2020), a plateau in the vertical synchrotron radiation profiles is found, which becomes more pronounced when the simulation runs with higher SFRs. In a low-frequency uGMRT follow-up study, Vijayan et al. (2022) find evidence for such a plateau in NGC 4631 at a 2–3 kpc height and suggest that the plateau might be attributed to CRE re-acceleration in shocks of the galactic outflow. However, we do not find clear evidence for the reported plateau in our data. On the contrary, we find that most of the substructure found in our low-frequency profiles start after 4 kpc. Another interesting observation is that we detect a much larger radio halo within our LOFAR 144 MHz data than shown by Vijayan et al. (2022), even though the spectral bands are comparable (this study: 144 MHz; Vijayan et al. 2022: 315 MHz). Additionally, the simulations by Vijayan et al. (2020) run for about 10 Myr, which might not be enough to result in an equilibrium state. Additionally, some of the assumptions made in the simulations might not apply.

To conclude this section, we note that the intensity and SPIX profiles analysed in this work show significant substructures at distances larger than ~2 kpc for NGC 891 and ~4 kpc for NGC 4631 that are yet not well explained by current model predictions. One possible line of explanation could be that variations in the SFR history change the parameters (gas density, CRE number density, and velocity) of the galactic wind and are therefore imprinted in the radio continuum profile. However, further studies and new models are needed to fully understand the structures found in the galactic halos.

8.3. Cosmic ray diffusion in NGC 4013?

Comparing our diffusion fitting results of NGC 4013 to the ST19 analysis, we find a higher diffusion coefficient (this study: $1.4 \times 10^{28} \, \mathrm{cm \, s^{-1}}$; ST19: $0.55–0.65 \times 10^{28} \, \mathrm{cm \, s^{-1}}$), a slightly lower injection index for the CREs (this study: 2.2; ST19: 2.6) and higher disk scale heights of the assumed exponential profile of the magnetic field (this study: 1.2 kpc; ST19: 0.1 kpc). The diffusion coefficients in the analysis of ST19 are based on VLA *L*- and *C*-band (6 GHz) data, which makes a direct comparison to our results more difficult as the CREs probed in this work are much older than the CREs traced by the higher-frequency measurements. Additionally, ST19 find advection to dominate when using 144 MHz and 1.6 GHz data for

the CR-transport analysis. However, we find much higher wind velocities (this study: ~150 km s⁻¹; ST19: 18−22 km s⁻¹). Following Recchia et al. (2016) and Heesen (2021), one can estimate the location where the transition from diffusion-dominated to advection-dominated CR-transport happens:

$$z_\star \approx 1.2 \frac{D/10^{28} \, \mathrm{cm^2 s^{-1}}}{v/100 \, \mathrm{km s^{-1}}} \, \mathrm{kpc}, \tag{18}$$

where D is the diffusion coefficient and v the advection wind speed. Using the diffusion coefficient from the UM and UL strips and the wind velocity of the LR and LM strips (taken from Tables 10 and 11), we find that the transition will happen at $z_\star = 1.5 \, \mathrm{kpc}$. Of course, this is only a zero-order estimate as we get the diffusion coefficients and wind velocities from different locations of the galaxy. The accuracy of the estimate is also affected by the relatively poor sampling of the radio halo, and because diffusion and advection profiles can only be reliably distinguished by analysing extended halo profiles (i.e. distinguishing between the two is difficult for small halos). ST19 report the position of this transition to be at $z_\star = 1−2 \, \mathrm{kpc}$[16], which is consistent with our estimate. Another galaxy that has been found to be diffusion-dominated is NGC 4565 (Heesen et al. 2019; Schmidt et al. 2019). While there is some scatter in the diffusion coefficients of this galaxy, our results fall in the same range. From the diffusion coefficient, one can derive the size of the diffusion halo L, if the CRE lifetime is known (adapted from Heesen 2021, Eq. (15)):

$$L = \sqrt{\frac{D \cdot \tau}{0.75 \times 10^{29}}} \, \mathrm{kpc}. \tag{19}$$

Here, D is the derived diffusion coefficient in units of $10^{28} \, \mathrm{cm^2 \, s^{-1}}$ and τ is the CRE lifetime, which is typically about 100 Myr for the energy range that is traced with the LOFAR HBA data. With this assumption we derive a diffusion halo size for NGC 4013 of $L = 4.3 \, \mathrm{kpc}$ (UR stripe excluded). A similar halo size is measured within our own Galaxy (Orlando & Strong 2013; Orlando 2018).

To summarise our results about NGC 4013, we note that our analysis remains inconclusive. Overall, the small extent of the galaxy halo makes it very difficult to analyse its CRE transport in great detail. New data reaching farther into the halo would be necessary in order to reliably distinguish the CRE transport mechanisms.

8.4. Advection-dominated galactic winds

Of the analysed sample, NGC 891 has been previously modelled with SPINNAKER advection models. Schmidt et al. (2019; SC19) analyse the radio halo of NGC 891 with 1.5 GHz and 6 GHz VLA CHANG-ES (+Effelsberg) data. They apply purely advective or diffusive transport models, but restrict the modelling region to a maximal height of 3 kpc. With the new LoTSS data and the newly cleaned CHANG-ES *L*-band data, we can now nearly double the extent of the modelling regions. Furthermore, we analyse six strips (three northern, three southern) instead of two strips (one northern, one southern). SC19 compare two models, one advection-dominated and one diffusion-dominated, and find that an advection model is a much better fit. With

---

[16] ST19 use a slightly modified version of Eq. (18), with a factor ranging from 0.3 to 0.6, instead of 1.2, which comes from different assumptions of the diffusion process. One-dimensional diffusion would lead to 0.3, while isotropic 3D diffusion leads to 1.2.

their advection model, they find a mid-plane wind velocity of $150 \, \text{km s}^{-1}$ for an accelerated galactic wind model. A direct comparison between the model used by SC19 and the flux tube model introduced by Heald et al. (2022) is difficult because the newer model includes additional processes (e.g. advection losses) and also because the modelling technique has changed. Nevertheless, we find similar velocities in proximity of the galactic disk, while we detect a split between central and outer strips farther out into the halo, where central strips have higher velocities than outer strips. Schmidt et al. (2019) predict that the galactic wind in NGC 891 reaches the halo escape velocity at a height of $9-17 \, \text{kpc}$. Our analysis does not allow a confirmation of their results. New, more sensitive data are needed to probe such scales. One might suspect that the UM strip does exceed the escape velocity in this range, as our model uncertainty allow for higher wind velocities compared to the escape velocity at heights larger than $7 \, \text{kpc}$, but this prediction remains uncertain.

As reported by MP19 and Vijayan et al. (2022), we expect advection to dominate the CR transport of NGC 4631. Nevertheless, we expect the wind to be much slower than estimated by MP19. MP19 estimate the wind to reach a velocity of $300 \, \text{km s}^{-1}$ at a height of $3 \, \text{kpc}$, which is much higher than the models in our analysis predict, although the uncertainties are high. Judging from our velocity profile, the galactic wind in NGC 4631 will reach the escape velocity much later (after $8 \, \text{kpc}$ in the UM strip, which has the fastest wind), compared to the prediction of MP19.

Comparing our results from the advection flux tube modelling to the analysis of NGC 5775 by Heald et al. (2022), our analysis of NGC 891, NGC 4157, and NGC 4631 points towards lower wind velocities. Heald et al. (2022) report wind velocities of more than $600 \, \text{km s}^{-1}$. However, NGC 5775 also has a much higher integrated SFR ($7.5 \, M_\odot \, \text{yr}^{-1}$) and also a higher SFR surface density ($9.4 \times 10^{-3} \, M_\odot \, \text{yr}^{-1} \, \text{kpc}^{-2}$) than the galaxies that we analysed, which most likely influences the CR-driven wind since these quantities can be interpreted as the driving source of the wind. Concerning the magnetic field strength profiles, we can confirm the results of Heald et al. (2022). As in the case of NGC 5775, the analysed galaxies generally show a good agreement between the modelled magnetic field strength profiles from SPINNAKER and the equipartition measurements. However, for heights above $6 \, \text{kpc}$, the model profiles of NGC 5775 deviate to lower field strength values compared to the equipartition measurements. We find a similar trend for the LM strip of NGC 891 at heights larger than $2 \, \text{kpc}$, which should be investigated in future studies.

Everett et al. (2008) analyse the galactic wind of the Milky Way by applying a hybrid wind model, where the wind is driven thermally as well as by CR pressure. They find an initial wind velocity of $v_0 = 173 \, \text{km s}^{-1}$ and the position of the critical point at a height of $z_c = 2.4 \, \text{kpc}$. At the critical point, they predict a sound speed $c_\star = 251 \, \text{km s}^{-1}$. From their model, Everett et al. (2008) expect the wind velocity to be rather constant until it reaches a height of approximately $1 \, \text{kpc}$ and then to accelerate quickly to surpass the sound speed. Therefore, the overall shape of the wind profile differs from the wind profiles shown in Fig. 11, where our velocity increases more gradually, and the predicted wind velocities for the Milky Way seem to lie between our predictions for NGC 4631 and NGC 891.

One of the key benefits of our study, compared to the analysis of NGC 5775 by Heald et al. (2022), is the chosen three-strip setup during box integration. This allows us to compare the properties of the galactic wind in the inner and outer part of

each galaxy. In Fig. 13, we present the difference of predicted magnetic field strength and wind velocity between the middle and the outer strips for NGC 891, NGC 4157, and NGC 4631. While we have not found a significant difference between middle and outer strips in the radio scale height analysis, we do see a split in the modelled wind velocity and magnetic field strength. Since the magnetic field strength at $z = 0$ is set as the average field strength from the equipartition measurement in each strip, there is an offset between the middle and outer strips. Interestingly, the magnetic field strength in the central regions declines faster than in the outer regions of the galaxy. This results in an approximate equality of the predicted magnetic field strength for high z values in central and outer strips. A similar behaviour is also visible in the cosmological magnetohydrodynamic simulations (Marinacci et al. 2018, Fig. 5) and simulations of isolated disk galaxies (Steinwandel et al. 2019, Fig. 2). With regard to wind velocity, the opposite behaviour can be observed. Here the difference in wind velocity between central and outer strips predominately increases (wind velocity increases faster in central strips than in outer ones) in the radio halo. For some strips of NGC 4631, central and outer wind velocities converge, but here the predicted uncertainties are very high.

9. Summary and outlook

In this paper we have reprocessed VLA L-band data in the D configuration and C configuration from the CHANG-ES project and combined them with newly published low-frequency data from LoTSS DR2 for an analysis of an edge-on galaxy sample. We investigated resolved non-thermal SPIX maps and intensity profiles perpendicular to the galactic disks, and we modelled the CR transport in the galactic halos. We demonstrated that new reduction techniques highly increase data quality, which allowed us to double the extent of the visible radio halo for most of the analysed galaxies. Additionally, we re-implemented the 'mixture-method' developed by Vargas et al. (2018) to estimate the resolved thermal emission of each galaxy and have made it publicly available using common python libraries. We then analysed the resolved non-thermal SPIX and radio scale heights. Lastly, we modelled the CR transport using the 1D advection and diffusion models of SPINNAKER. Our main results can be summarised as follows:

1. We find that the LoTSS DR2 maps are affected by thermal absorption within the galactic disk, especially in star-forming regions, as the non-thermal SPIX maps exceed the expected limit for freshly induced CREs of $\alpha_{\text{nth}} = -0.6$ in these areas.
2. The scale height analysis based on the model comparison with the AICc shows that most of the profiles are equally well fitted with one-component exponential models as with two-component ones. Additionally, we find substructures in the intensity and SPIX profiles that are not well explained by contemporary CRE transport models.
3. We do not find a strong correlation between the radio halo scale height and physical properties, such as galactic diameter, gravitational potential, SFR, SFR surface density, sSFR, and magnetic field strength measured within the galactic disk.
4. The modelling of the galactic wind indicates a split of magnetic field strength and wind velocity in the immediate vicinity of the galactic disks for inner and outer strips of the galaxy. While the difference in magnetic field strength evens out in the radio halo, the difference in wind speed increases.
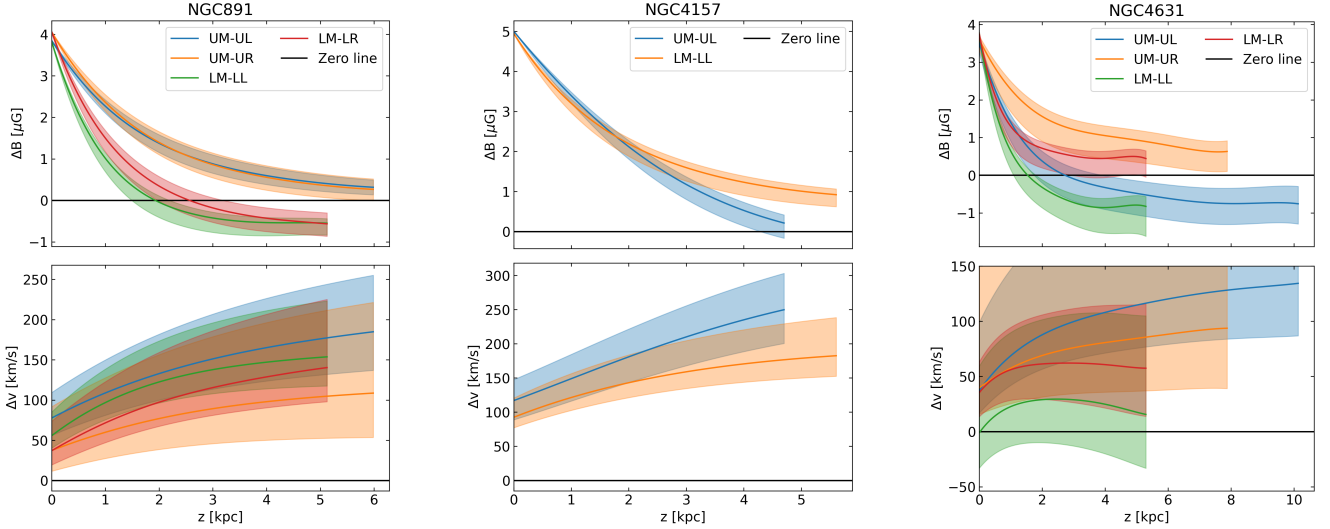
Fig. 13. Difference of magnetic field strength (top row) and wind velocity (bottom row) between central and outer, left and right, strips for NGC 891 (left column), NGC 4157 (middle column), and NGC 4631 (right column). Black lines indicate equal magnetic field strengths/wind velocities in the central and outer strips.

In this paper we have successfully analysed the CRE transport of NGC 891, NGC 4157, and NGC 4631, while the analysis of NGC 3432 and NGC 4013 remains inconclusive. Our results suggest that there are significant differences in CR transport depending on the location within the galactic disk, which should be accounted for in future CRE transport models. To better understand the CRE transport within the radio halo of NGC 4013, a possible approach would be to also include higher-frequency data, as done by Stein et al. (2019a), to trace the younger CREs in the halo and then simultaneously fit three frequencies within SPINNAKER. Adding a third frequency to the analysis would lead to higher precision of the model predictions, as it increases the number of profiles that are fitted by SPINNAKER from three (two intensities, one SPIX) to five (three intensities, two SPIXes). However, the relatively small extent of the radio halo of NGC 4013 will most likely always be a limiting factor for CR transport analysis. Adding information about the magnetic field structure from polarisation measurements and implementing it in new CRE transport models would further help in better understanding the role of CRs within galactic feedback processes. More detailed modelling approaches are certainly needed and will be possible as Square Kilometre Array Observatory (SKAO) precursors and pathfinders, and eventually the SKAO itself, enable us to analyse CR transport within galaxies on an unprecedented scale, in terms of both sensitivity and resolution.

2013) is the Low Frequency Array designed and constructed by ASTRON. It has observing, data processing, and data storage facilities in several countries, which are owned by various parties (each with their own funding sources), and which are collectively operated by the ILT foundation under a joint scientific policy. The efforts of the LSKSP have benefited from funding from the European Research Council, NOVA, NWO, CNRS-INSU, the SURF Co-operative, the UK Science and Technology Funding Council, the Ministry of Science and Higher Education, Poland, and the Jülich Supercomputing Centre. The following software packages have been used in this work: Astropy (Astropy Collaboration 2013, 2018). This research has made use of "Aladin sky atlas" developed at CDS, Strasbourg Observatory, France (Bonnarel et al. 2000; Boch & Fernique 2014); SAOImage DS9 (Joye & Mandel 2003).

References

Adebahr, B., Krause, M., Klein, U., et al. 2013, A&A, 555, A23
Akaike, H. 1998, Selected Papers of Hirotugu Akaike, 199
Aniano, G., Draine, B. T., Gordon, K. D., & Sandstrom, K. 2011, PASP, 123, 1218
Astropy Collaboration (Robitaille, T. P., et al.) 2013, A&A, 558, A33
Astropy Collaboration (Price-Whelan, A. M., et al.) 2018, AJ, 156, 123
Basu, A., Beck, R., Schmidt, P., & Roy, S. 2015, MNRAS, 449, 3879
Beck, R., & Graeve, R. 1982, A&A, 105, 192
Beck, R., & Krause, M. 2005, Astron. Nachr., 326, 414
Blasi, P., Amato, E., & Serpico, P. D. 2012, Phys. Rev. Lett., 109, 061101
Boch, T., & Fernique, P. 2014, in Astronomical Data Analysis Software and Systems XXIII, eds. N. Manset, & P. Forshay, ASP Conf. Ser., 485, 277
Bonnarel, F., Fernique, P., Bienaymé, O., et al. 2000, A&AS, 143, 33
Boucaud, A. 2016, https://doi.org/10.5281/zenodo.61392
Boucaud, A., Bocchio, M., Abergel, A., et al. 2016, A&A, 596, A63
Breitschwerdt, D., McKenzie, J. F., & Voelk, H. J. 1991, A&A, 245, 79
Bulanov, S. V., & Dogel, V. A. 1974, Ap&SS, 29, 305
Butsky, I. S., & Quinn, T. R. 2018, ApJ, 868, 108
Butsky, I. S., Fielding, D. B., Hayward, C. C., et al. 2020, ApJ, 903, 77
Calzetti, D., Kennicutt, R. C., Engelbracht, C. W., et al. 2007, ApJ, 666, 870
Carilli, C. L., & Barthel, P. D. 1996, A&ARv, 7, 1
Chyży, K. T., Weżgowiec, M., Beck, R., & Bomans, D. J. 2011, A&A, 529, A94
Cummings, A. C., Stone, E. C., Heikkila, B. C., et al. 2016, ApJ, 831, 18
Daigle, O., Carignan, C., Amram, P., et al. 2006, MNRAS, 367, 469
Dicaire, I., Carignan, C., Amram, P., et al. 2008, MNRAS, 385, 553
Dörner, J., Reichherzer, P., Becker Tjus, J., & Heesen, V. 2023, A&A, 669, A111
Dumke, M., Krause, M., Wielebinski, R., & Klein, U. 1995, A&A, 302, 691
Everett, J. E., Zweibel, E. G., Benjamin, R. A., et al. 2008, ApJ, 674, 258
Evoli, C., Blasi, P., Morlino, G., & Aloisio, R. 2018, Phys. Rev. Lett., 121, 021102
Girichidis, P., Naab, T., Walch, S., et al. 2016, ApJ, 816, L19
Hafen, Z., Faucher-Giguère, C.-A., Anglés-Alcázar, D., et al. 2019, MNRAS, 488, 1248

Heald, G., Józsa, G., Serra, P., et al. 2011, A&A, 526, A118
Heald, G. H., Heesen, V., Sridhar, S. S., et al. 2022, MNRAS, 509, 658
Heckman, T. M., Alexandroff, R. M., Borthakur, S., Overzier, R., & Leitherer, C. 2015, ApJ, 809, 147
Heesen, V. 2021, Ap&SS, 366, 117
Heesen, V., Dettmar, R.-J., Krause, M., Beck, R., & Stein, Y. 2016, MNRAS, 458, 332
Heesen, V., Croston, J. H., Morganti, R., et al. 2018a, MNRAS, 474, 5049
Heesen, V., Krause, M., Beck, R., et al. 2018b, MNRAS, 476, 158
Heesen, V., Whitler, L., Schmidt, P., et al. 2019, A&A, 628, L3
Heesen, V., Klocke, T. L., Brüggen, M., et al. 2022a, A&A, 669, A8
Heesen, V., Staffehl, M., Basu, A., et al. 2022b, A&A, 664, A83
Irwin, J., Beck, R., Benjamin, R. A., et al. 2012, AJ, 144, 43
Irwin, J., Wiegert, T., Merritt, A., et al. 2019, AJ, 158, 21
Jarrett, T. H., Masci, F., Tsai, C. W., et al. 2012, AJ, 144, 68
Jarrett, T. H., Cluver, M. E., Brown, M. J. I., et al. 2019, ApJS, 245, 25
Ji, S., Chan, T. K., Hummels, C. B., et al. 2020, MNRAS, 496, 4221
Joye, W. A., & Mandel, E. 2003, in Astronomical Data Analysis Software and Systems XII, eds. H. E. Payne, R. I. Jedrzejewski, & R. N. Hook, ASP Conf. Ser., 295, 489
Kantharia, N. G., Ananthakrishnan, S., Nityananda, R., & Hota, A. 2005, A&A, 435, 483
Kellermann, K. I., Pauliny-Toth, I. I. K., & Williams, P. J. S. 1969, ApJ, 157, 1
Klein, U., Beck, R., Buczilowski, U. R., & Wielebinski, R. 1982, A&A, 108, 176
Klein, U., Lisenfeld, U., & Verley, S. 2018, A&A, 611, A55
Krause, M., Irwin, J., Wiegert, T., et al. 2018, A&A, 611, A72
Lazarian, A., & Xu, S. 2021, ApJ, 923, 53
Lerche, I., & Schlickeiser, R. 1980, ApJ, 239, 1089
Lerche, I., & Schlickeiser, R. 1982, A&A, 107, 148
Li, J.-T., Beck, R., Dettmar, R.-J., et al. 2016, MNRAS, 456, 1723
Limousin, M., Kneib, J. P., Bardeau, S., et al. 2007, A&A, 461, 881
Marinacci, F., Vogelsberger, M., Pakmor, R., et al. 2018, MNRAS, 480, 5113
McMullin, J. P., Waters, B., Schiebel, D., Young, W., & Golap, K. 2007, in Astronomical Data Analysis Software and Systems XVI, eds. R. A. Shaw, F. Hill, & D. J. Bell, ASP Conf. Ser., 376, 127
Miskolczi, A., Heesen, V., Horellou, C., et al. 2019, A&A, 622, A9
Mohan, N., & Rafferty, D. 2015, PyBDSF: Python Blob Detection and Source Finder
Mora-Partiarroyo, S. C., Krause, M., Basu, A., et al. 2019, A&A, 632, A10
Mulcahy, D. D., Horneffer, A., Beck, R., et al. 2018, A&A, 615, A98
Müller, P., Krause, M., Beck, R., & Schmidt, P. 2017a, NOD3: Single dish reduction software
Müller, P., Krause, M., Beck, R., & Schmidt, P. 2017b, A&A, 606, A41
Murphy, E. J., Condon, J. J., Schinnerer, E., et al. 2011, ApJ, 737, 67
Offringa, A. R., McKinley, B., Hurley-Walker, N., et al. 2014, MNRAS, 444, 606
Orlando, E. 2018, MNRAS, 475, 2724

Orlando, E., & Strong, A. 2013, MNRAS, 436, 2127
Osterbrock, D. E., & Ferland, G. J. 2006, Astrophysics of Gaseous Nebulae and Active Galactic Nuclei
Otte, B., & Dettmar, R. J. 1999, A&A, 343, 705
Pakmor, R., Gómez, F. A., Grand, R. J. J., et al. 2017, MNRAS, 469, 3185
Prada, F., Vitvitska, M., Klypin, A., et al. 2003, ApJ, 598, 260
Quataert, E., Thompson, T. A., & Jiang, Y.-F. 2022a, MNRAS, 510, 1184
Quataert, E., Jiang, F., & Thompson, T. A. 2022b, MNRAS, 510, 920
Recchia, S., Blasi, P., & Morlino, G. 2016, MNRAS, 462, 4227
Salem, M., & Bryan, G. L. 2014, MNRAS, 437, 3312
Schmidt, P., Krause, M., Heesen, V., et al. 2019, A&A, 632, A12
Shimwell, T. W., Röttgering, H. J. A., Best, P. N., et al. 2017, A&A, 598, A104
Shimwell, T. W., Tasse, C., Hardcastle, M. J., et al. 2019, A&A, 622, A1
Shimwell, T. W., Hardcastle, M. J., Tasse, C., et al. 2022, A&A, 659, A1
Somerville, R. S., Behroozi, P., Pandya, V., et al. 2018, MNRAS, 473, 2714
Stein, Y., Dettmar, R. J., Weżgowiec, M., et al. 2019a, A&A, 632, A13
Stein, Y., Dettmar, R. J., Irwin, J., et al. 2019b, A&A, 623, A33
Steinwandel, U. P., Beck, M. C., Arth, A., et al. 2019, MNRAS, 483, 1008
Strong, A. W. 1978, A&A, 66, 205
Strong, A. W., Moskalenko, I. V., & Ptuskin, V. S. 2007, Ann. Rev. Nucl. Part. Sci., 57, 285
Su, M., Slatyer, T. R., & Finkbeiner, D. P. 2010, ApJ, 724, 1044
Tabatabaei, F. S., Beck, R., Krügel, E., et al. 2007, A&A, 475, 133
Tabatabaei, F. S., Schinnerer, E., Krause, M., et al. 2017, ApJ, 836, 185
Tabatabaei, F. S., Minguez, P., Prieto, M. A., & Fernández-Ontiveros, J. A. 2018, Nat. Astron., 2, 83
Thornbury, A., & Drury, L. O. 2014, MNRAS, 442, 3010
Tumlinson, J., Peeples, M. S., & Werk, J. K. 2017, ARA&A, 55, 389
Uhlig, M., Pfrommer, C., Sharma, M., et al. 2012, MNRAS, 423, 2374
van de Voort, F., Bieri, R., Pakmor, R., et al. 2021, MNRAS, 501, 4888
van der Hulst, J. M., & Hummel, E. 1985, A&A, 150, L7
van Haarlem, M. P., Wise, M. W., Gunst, A. W., et al. 2013, A&A, 556, A2
van Weeren, R. J., Shimwell, T. W., Botteon, A., et al. 2021, A&A, 651, A115
Varenius, E., Conway, J. E., Martí-Vidal, I., et al. 2015, A&A, 574, A114
Vargas, C. J., Mora-Partiarroyo, S. C., Schmidt, P., et al. 2018, ApJ, 853, 128
Vargas, C. J., Walterbos, R. A. M., Rand, R. J., et al. 2019, ApJ, 881, 26
Veilleux, S., Cecil, G., & Bland-Hawthorn, J. 2005, ARA&A, 43, 769
Vijayan, A., Nath, B. B., Sharma, P., & Shchekinov, Y. 2020, MNRAS, 492, 2924
Vijayan, A., Dwarakanath, K. S., Nath, B. B., & Kale, R. 2022, MNRAS, 511, 3150
Wiegert, T., Irwin, J., Miskolczi, A., et al. 2015, AJ, 150, 81
Wiegert, T., Irwin, J., Miskolczi, A., et al. 2017, AJ, 153, 202
Wiener, J., Pfrommer, C., & Oh, S. P. 2017, MNRAS, 467, 906
Wills, K. A., Pedlar, A., Muxlow, T. W. B., & Wilkinson, P. N. 1997, MNRAS, 291, 517
Zweibel, E. G. 2013, Phys. Plasmas, 20, 055501
Zweibel, E. G. 2017, Phys. Plasmas, 24, 055402

Appendix A: Thermal fraction maps

The thermal emission maps in for the VLA L-band and LOFAR HBA data as well as the corresponding thermal fraction maps are displayed in this section. In the thermal fraction maps, we plot contours at factors of 0.25, 0.5, and 0.75 of the peak thermal fraction that was measured for each galaxy.
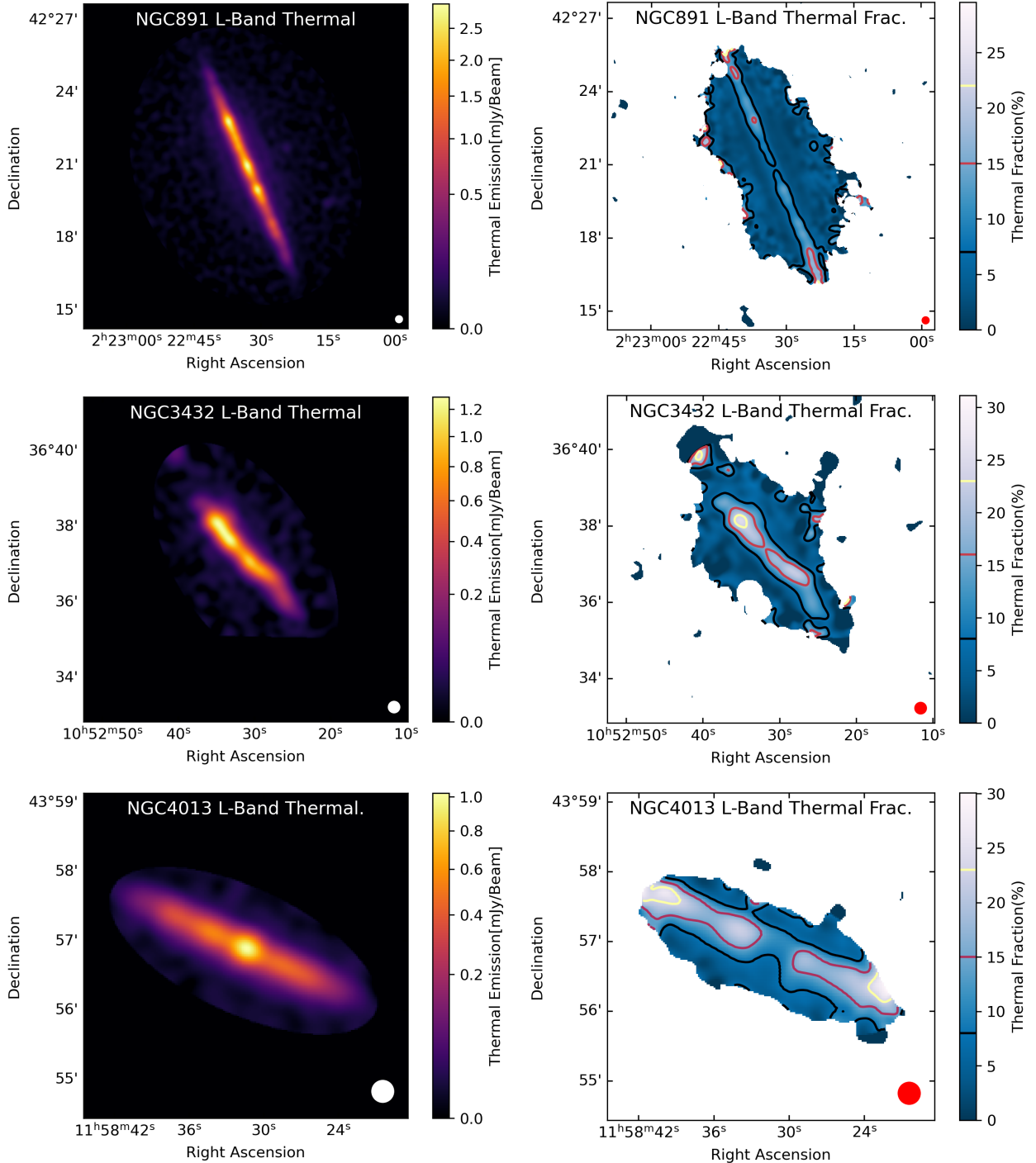

Fig. A.1. Thermal emission at 1.5 GHz (CHANG-ES L band) (left column) and thermal fraction maps of the L-band data (right column) of NGC 891 (top row), NGC 3432 (middle row), and NGC 4013 (bottom row). Thermal emission maps use a power law scaling with a power law index of 0.5. Thermal fraction maps are clipped below 3σ above the background noise. The beam is displayed in the bottom-right corner of each map as a white (thermal emission maps) or red (thermal fraction maps) circle.
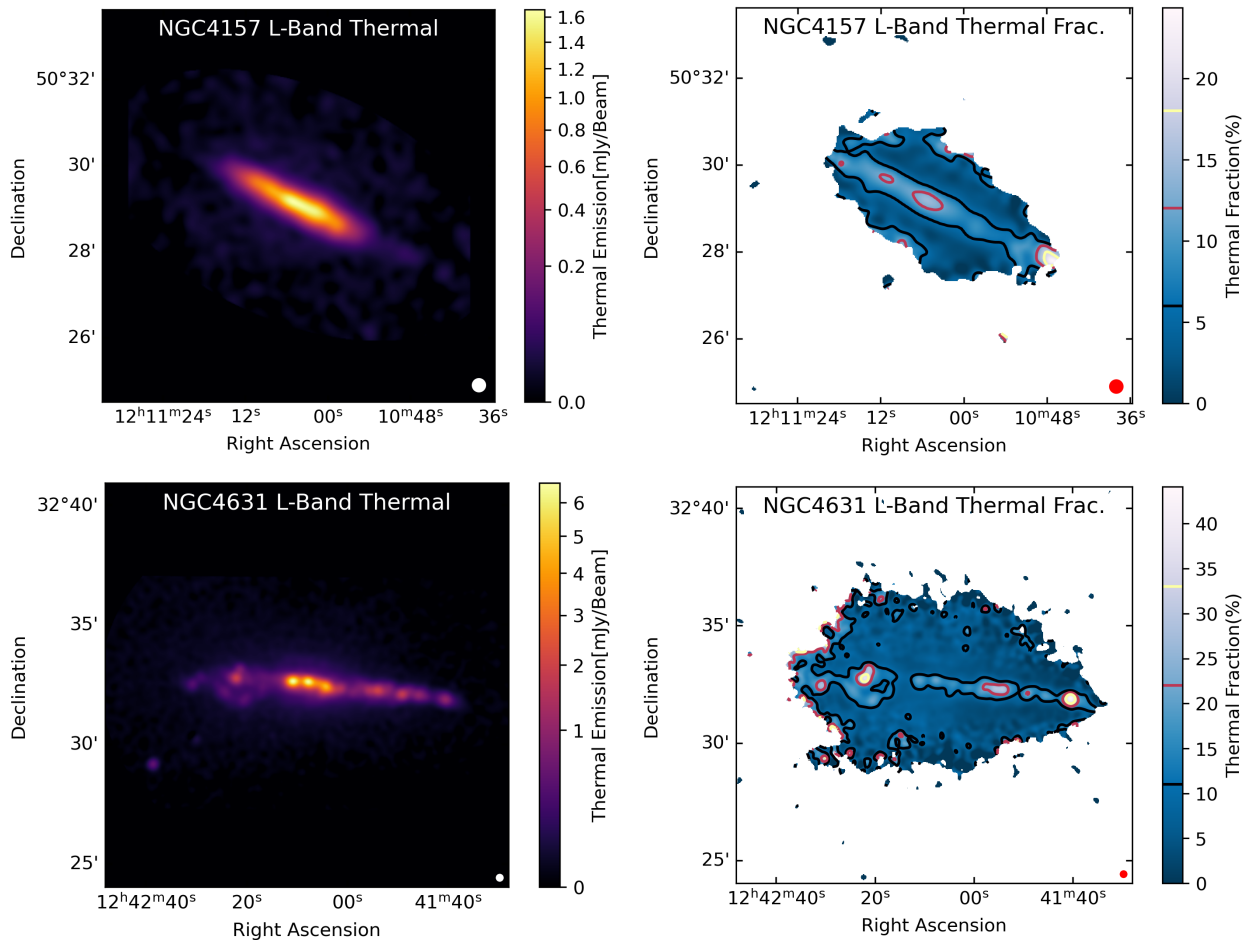
Fig. A.2. Fig. A.1 continued: Thermal emission at 1.5 GHz (CHANG-ES L band) (left column) and thermal fraction maps of the L-band data (right column) of NGC 4157 (top row) and NGC 4631 (bottom row).
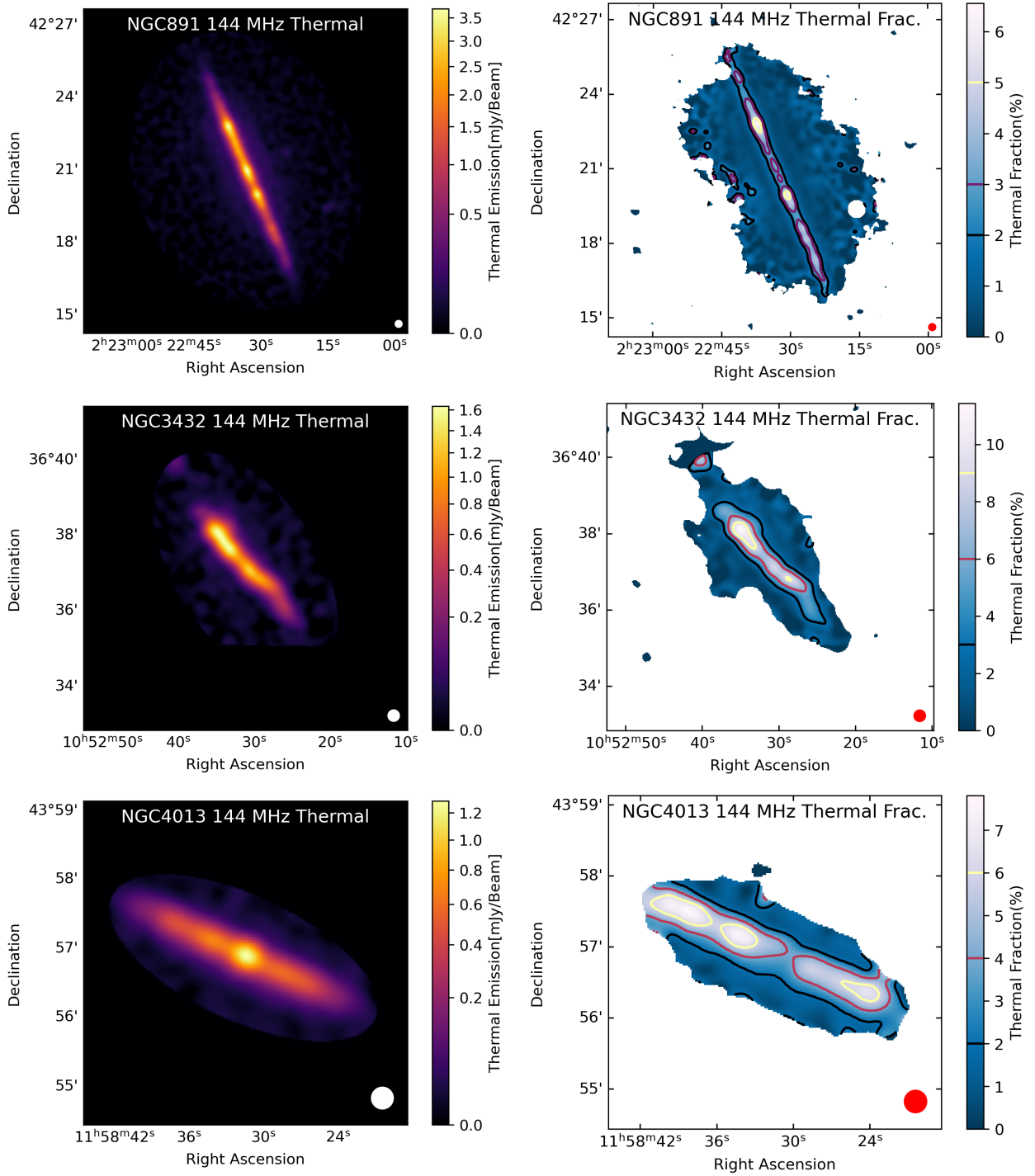
Fig. A.3. Thermal emission at 144 MHz (LOFAR HBA) (left column) and thermal fraction maps of the HBA data (right column) of NGC 891 (top row), NGC 3432 (middle row), and NGC 4013 (bottom row). Thermal emission maps use a power law scaling with a power law index of 0.5. Thermal fraction maps are clipped below 3σ above the background noise. The beam is displayed in the bottom-right corner of each map as a white (thermal emission maps) or red (thermal fraction maps) circle.
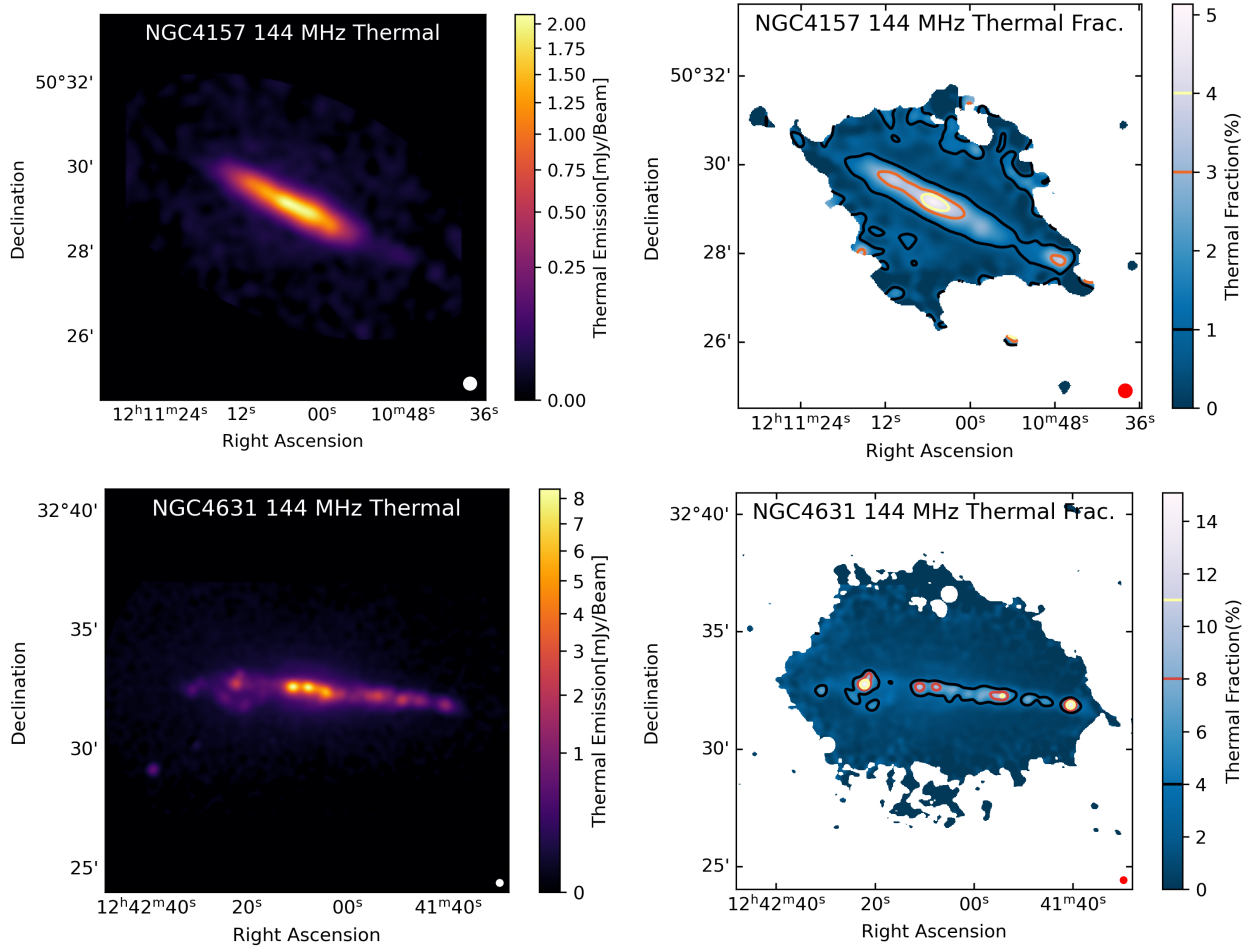
Fig. A.4. Fig. A.3 continued: Thermal emission at 144 MHz (LOFAR HBA) (left column) and thermal fraction maps of the HBA data (right column) of NGC 4157 (top row), and NGC 4631 (bottom row).

Appendix B: Intensity profiles

In this section we present the best-fitting model parameters from χ^2-minimisation for one- and two-component exponential profiles. The model comparison was performed with the AICc in Table B.1. Four models were tested (listed from fewest to most free model parameters): one-component exponential without off-set in the z direction (one_fo), one-component exponential with offset in the z direction (one), two-component exponential without offset in the z direction (two_fo), and two-component exponential with offset in the z direction (two). We also display the intensity profiles from the box-integration technique for the LOFAR HBA and VLA L band as well as the best-fitting (based on the AICc model comparison) model as a black dashed line.

Table B.1. Parameters from box integration model fitting: galaxy name, frequency of fitted data, model identifier, strip identifier, intensity and scale height of the first exponential component, intensity and scale height of the second exponential component (if applicable), offset in the z direction (if applicable), reduced χ-square.

| Galaxy	ν [MHz]	Model	ID	w_0 [μ Jy Beam^{-1}]	z_0 [kpc]	w_1 [μ Jy Beam^{-1}]	z_1 [kpc]	Z_0 [kpc]	χ^2_ν
N 3432	1500	one_fo	LR	0.32±0.04	1.16±0.09	-	-	-	3.72
N 3432	144	one_fo	LR	7.5±2.3	0.28±0.07	-	-	-	2.41
N 3432	1500	one	UR	2.20±0.20	0.45±0.03	-	-	0.54±0.07	4.27
N 3432	144	one	UR	31±21	0.13±0.09	-	-	0.72±0.06	1.39
N 3432	1500	one_fo	LM	4.68±0.27	0.940±0.028	-	-	-	5.23
N 3432	144	one_fo	LM	16.7±1.3	1.01±0.04	-	-	-	1.11
N 3432	1500	one_fo	UM	4.43±0.21	0.789±0.019	-	-	-	10.07
N 3432	144	one_fo	UM	16.7±1.2	0.87±0.03	-	-	-	2.26
N 3432	1500	one_fo	LL	2.47±0.29	0.91±0.05	-	-	-	1.44
N 3432	144	one_fo	LL	8.0±1.0	1.14±0.07	-	-	-	1.77
N 3432	1500	one_fo	UL	1.55±0.16	0.91±0.05	-	-	-	1.97
N 3432	144	one_fo	UL	6.2±0.8	1.03±0.07	-	-	-	1.50
N 4013	1500	one_fo	LR	2.09±0.20	0.607±0.027	-	-	-	1.77
N 4013	144	one_fo	LR	9.6±1.0	0.75±0.04	-	-	-	0.55
N 4013	1500	one_fo	UR	2.32±0.22	0.73±0.04	-	-	-	0.83
N 4013	144	one_fo	UR	12.4±1.4	0.69±0.04	-	-	-	0.12
N 4013	1500	one_fo	LM	4.7±0.5	0.526±0.025	-	-	-	8.92
N 4013	144	one_fo	LM	20.6±2.1	0.639±0.026	-	-	-	3.15
N 4013	1500	one_fo	UM	9.4±0.9	0.476±0.018	-	-	-	0.97
N 4013	144	one_fo	UM	33±3	0.614±0.023	-	-	-	0.30
N 4013	1500	one_fo	LL	2.45±0.18	0.670±0.030	-	-	-	2.89
N 4013	144	one_fo	LL	10.0±1.0	0.74±0.04	-	-	-	1.41
N 4013	1500	one_fo	UL	3.41±0.22	0.578±0.020	-	-	-	1.11
N 4013	144	one_fo	UL	8.8±0.8	1.05±0.05	-	-	-	5.63
N 4157	1500	one_fo	LR	3.2±0.4	1.32±0.07	-	-	-	0.68
N 4157	144	one	LR	15.7±2.3	1.25±0.07	-	-	0.55±0.26	5.26
N 4157	1500	one_fo	UR	3.7±0.6	0.96±0.06	-	-	-	0.17
N 4157	144	one_fo	UR	6.9±1.2	2.31±0.19	-	-	-	6.10
N 4157	1500	one_fo	LM	13.6±0.6	1.121±0.021	-	-	-	4.79
N 4157	144	two_fo	LM	66±7	0.88±0.11	8.6±2.0	3.5±0.3	-	2.34
N 4157	1500	two_fo	UM	8±7	0.7±0.4	9±8	1.25±0.20	-	0.65
N 4157	144	two	UM	64±5	1.21±0.10	1.3±0.6	10±5	0.24±0.17	2.88
N 4157	1500	one_fo	LL	2.6±0.4	0.96±0.08	-	-	-	0.03
N 4157	144	one_fo	LL	5.0±0.8	2.63±0.19	-	-	-	4.17
N 4157	1500	one_fo	UL	2.4±0.3	1.45±0.07	-	-	-	2.24
N 4157	144	one_fo	UL	10.0±1.1	2.59±0.13	-	-	-	0.40
N 4631	1500	one_fo	LR	6.8±0.4	1.053±0.029	-	-	-	1.11
N 4631	144	one_fo	LR	19.4±1.1	1.89±0.05	-	-	-	0.74
N 4631	1500	two	UR	10.5±2.8	0.52±0.16	0.89±0.22	2.6±0.3	-0.6±0.4	0.39
N 4631	144	two_fo	UR	11.6±1.3	1.44±0.27	2.7±1.2	4.5±0.8	-	1.07
N 4631	1500	two	LM	42±16	0.59±0.10	6.3±1.2	1.80±0.07	-0.7±0.4	1.88
N 4631	144	two_fo	LM	37.0±2.9	1.46±0.12	3.0±1.0	5.3±0.7	-	5.03
N 4631	1500	two	UM	45±10	0.39±0.11	5.0±0.6	2.01±0.05	-0.44±0.27	1.68
N 4631	144	one_fo	UM	19.1±0.8	2.90±0.05	-	-	-	4.45
N 4631	1500	one_fo	LL	2.00±0.14	1.93±0.06	-	-	-	1.12
N 4631	144	one_fo	LL	8.6±0.5	2.84±0.07	-	-	-	0.86
N 4631	1500	one_fo	UL	1.15±0.09	2.15±0.09	-	-	-	1.07
N 4631	144	one_fo	UL	6.1±0.3	3.71±0.10	-	-	-	0.75
N 891	1500	one_fo	LR	4.3±0.3	1.09±0.04	-	-	-	2.55
N 891	144	one_fo	LR	15.2±1.0	1.85±0.04	-	-	-	4.02
N 891	1500	one_fo	UR	4.5±0.3	1.35±0.04	-	-	-	3.50
N 891	144	two_fo	UR	32±5	0.77±0.15	6.7±1.4	3.04±0.26	-	3.41
N 891	1500	one_fo	LM	17.2±0.8	0.822±0.016	-	-	-	7.41
N 891	144	two	LM	188±113	0.87±0.08	5.8±2.1	2.9±0.4	-1.0±0.7	1.01
N 891	1500	one_fo	UM	16.9±0.6	1.176±0.014	-	-	-	5.88
N 891	144	two	UM	111±18	1.05±0.10	6.6±2.3	3.6±0.5	-0.33±0.27	0.50
N 891	1500	one_fo	LL	7.4±0.6	1.05±0.03	-	-	-	1.21
N 891	144	two_fo	LL	43±22	0.37±0.21	13.9±1.6	2.18±0.08	-	1.22
N 891	1500	one_fo	UL	6.9±0.6	1.07±0.04	-	-	-	1.05
N 891	144	one_fo	UL	25.4±1.9	1.67±0.05	-	-	-	1.05
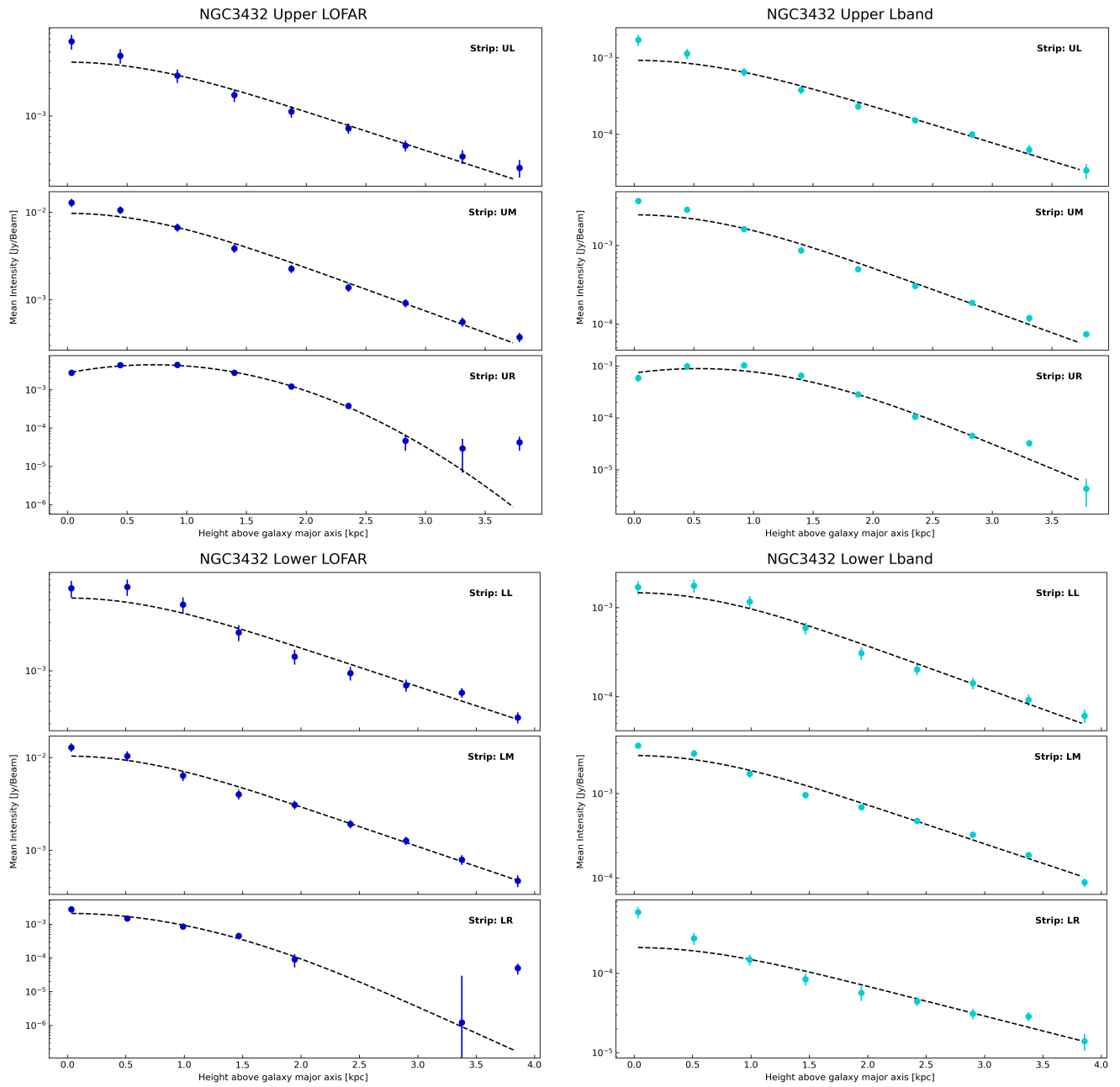
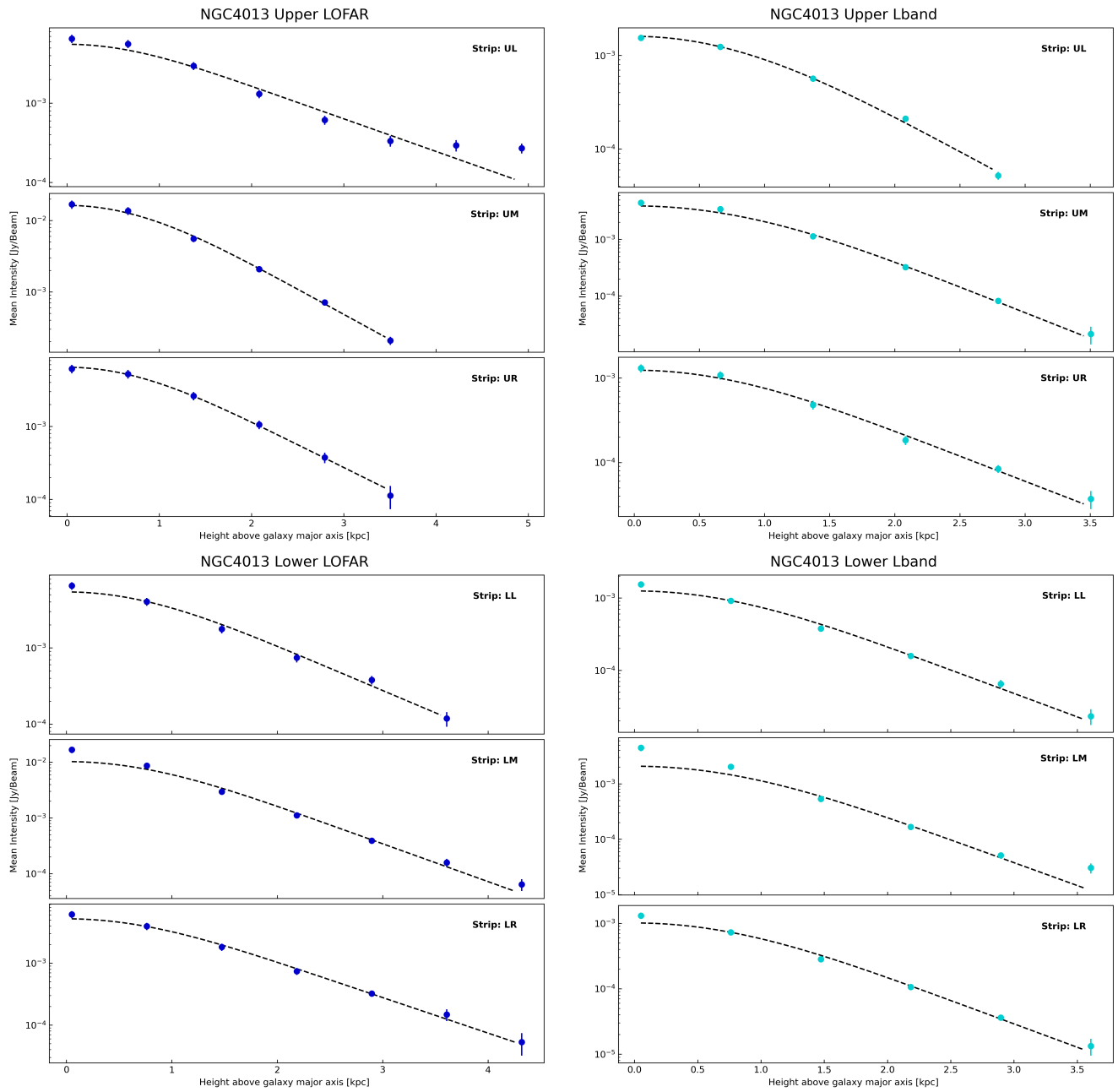**Fig. B.1.** Intensity profiles of NGC 3432

Fig. B.2. Intensity profiles of NGC 4013

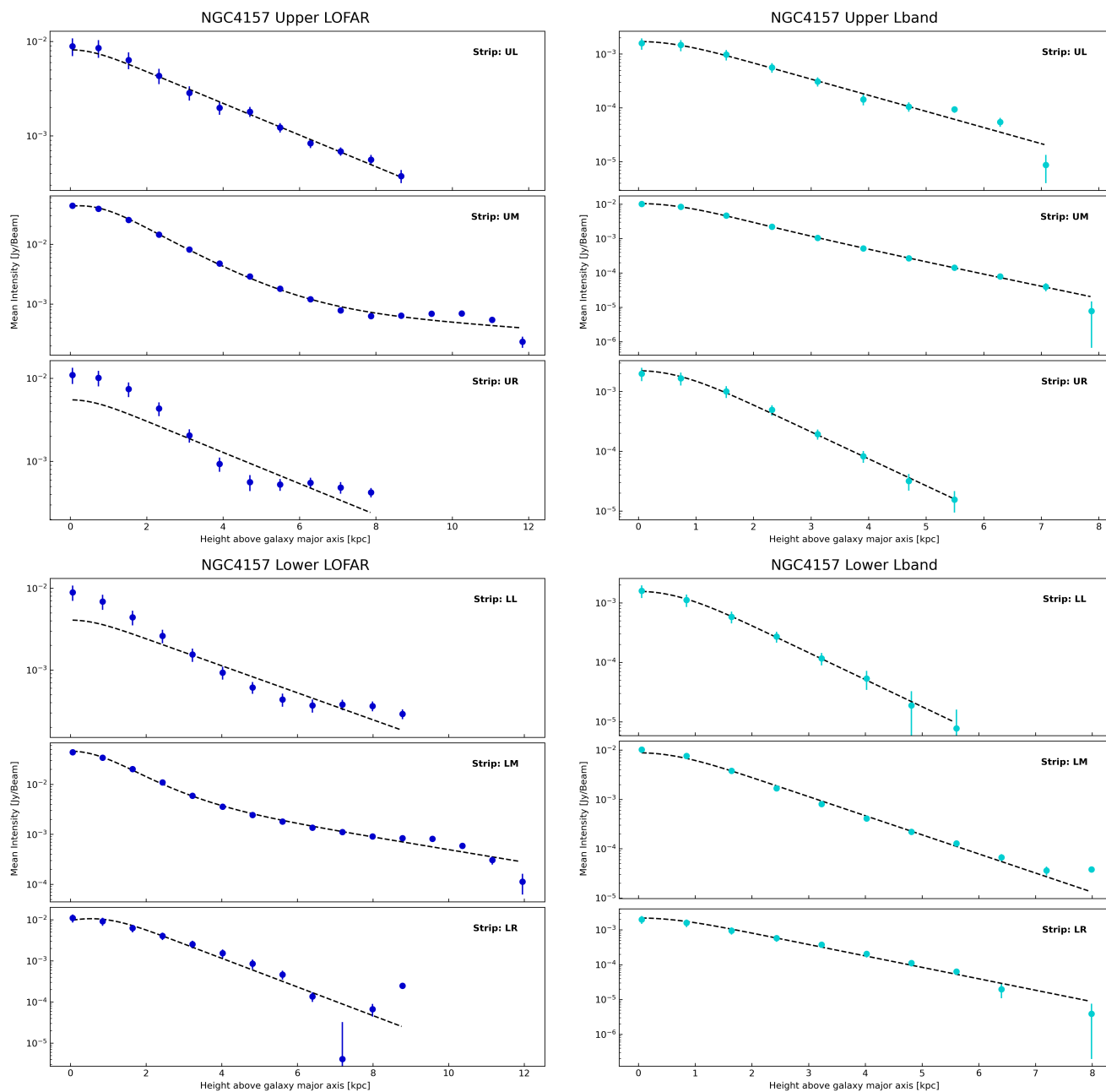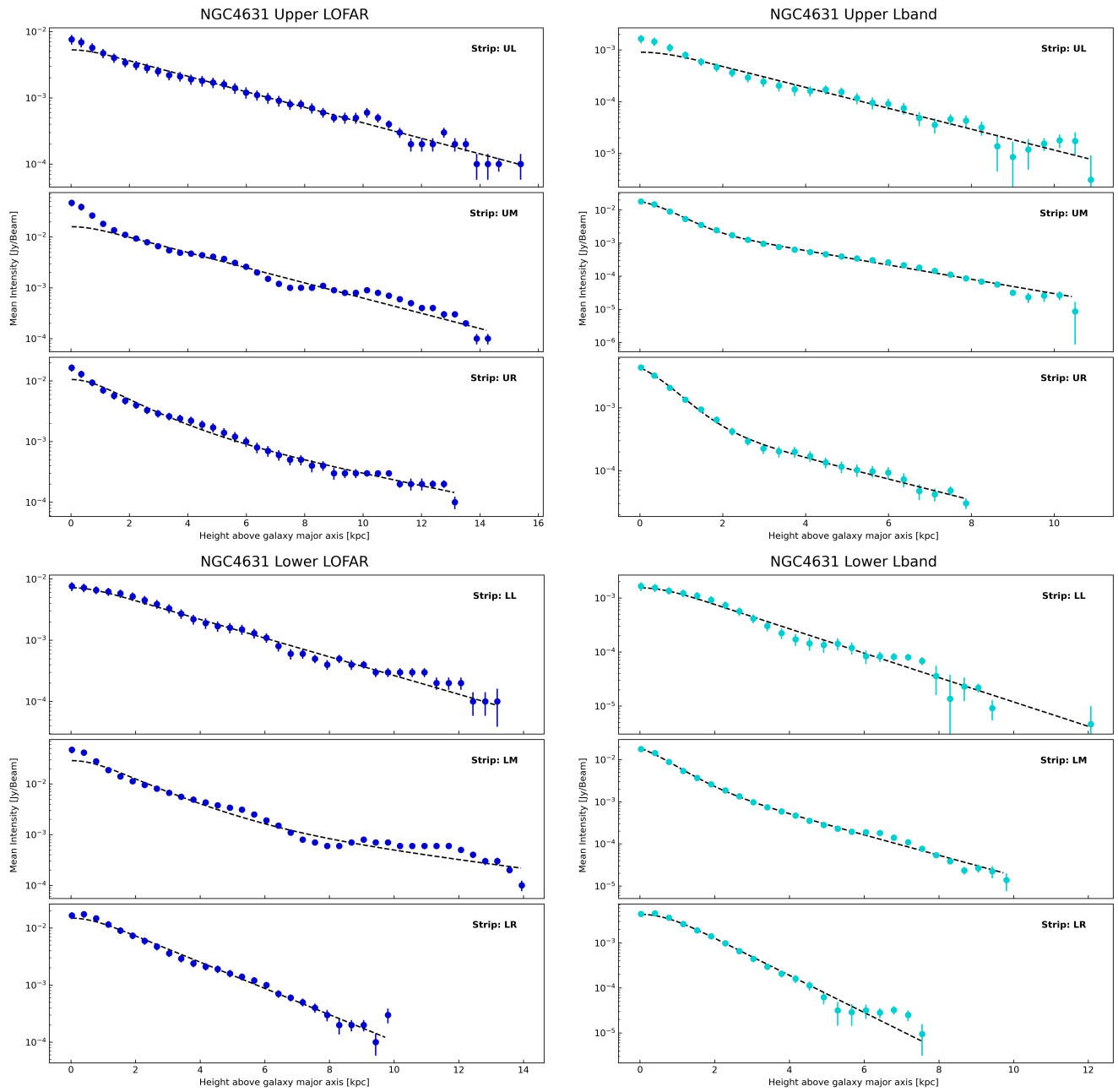**Fig. B.3.** Intensity profiles of NGC 4157

Fig. B.4. Intensity profiles of NGC 4631

Appendix C: SPINNAKER profiles

Best-fitting SPINNAKER models (advection or diffusion) for all galaxies (NGC 891, NGC 3432, NGC 4013, NGC 4157, and NGC 4631) are displayed in this section. The structure of the SPINNAKER output is explained in Fig. 10.
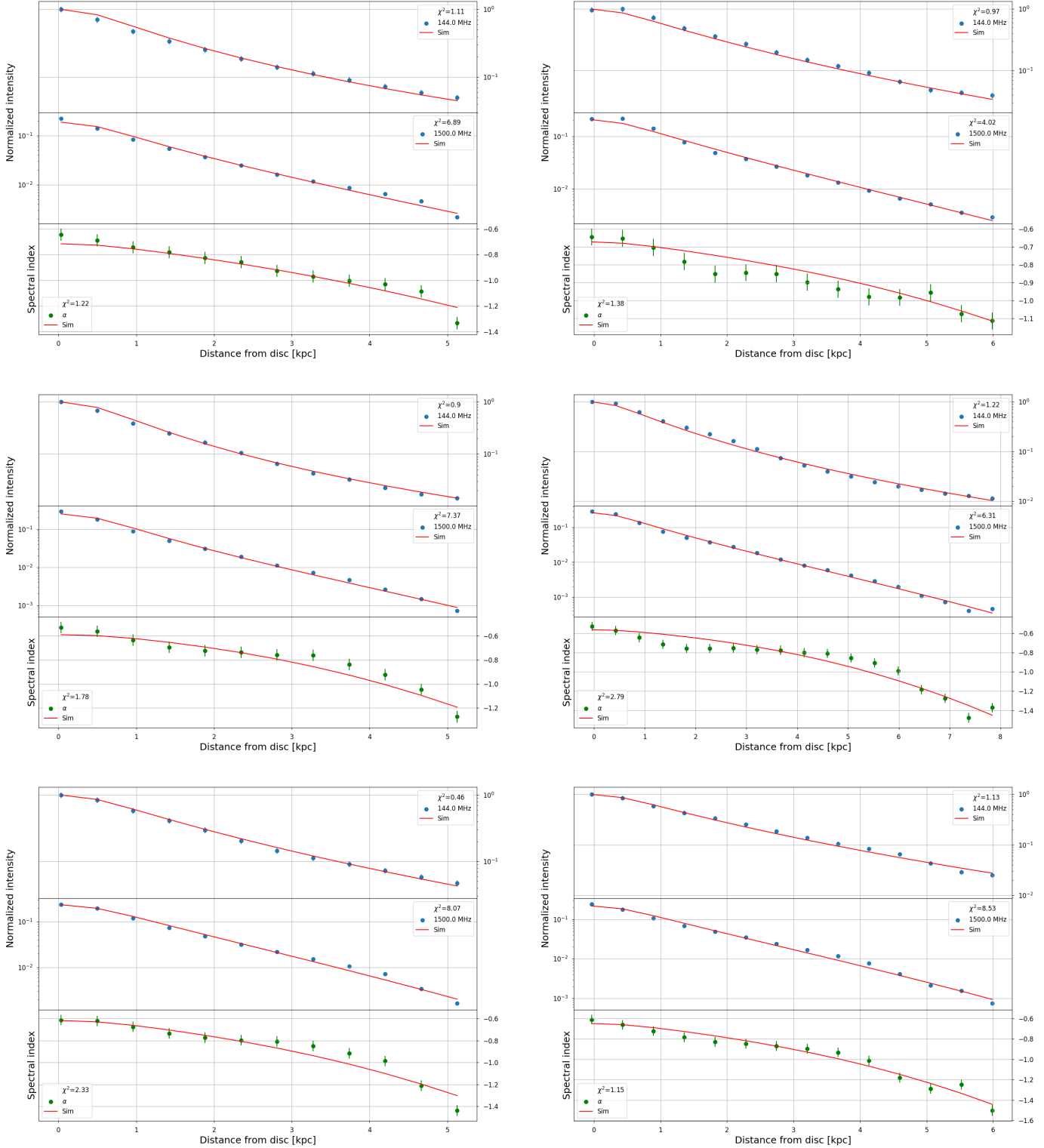

Fig. C.1. SPINNAKER profiles of NGC 891 (all advection). Strips are presented as follows: top left: LR, top right: UR, middle left: LM, middle right: UM, bottom left: LL, and bottom right: UL.
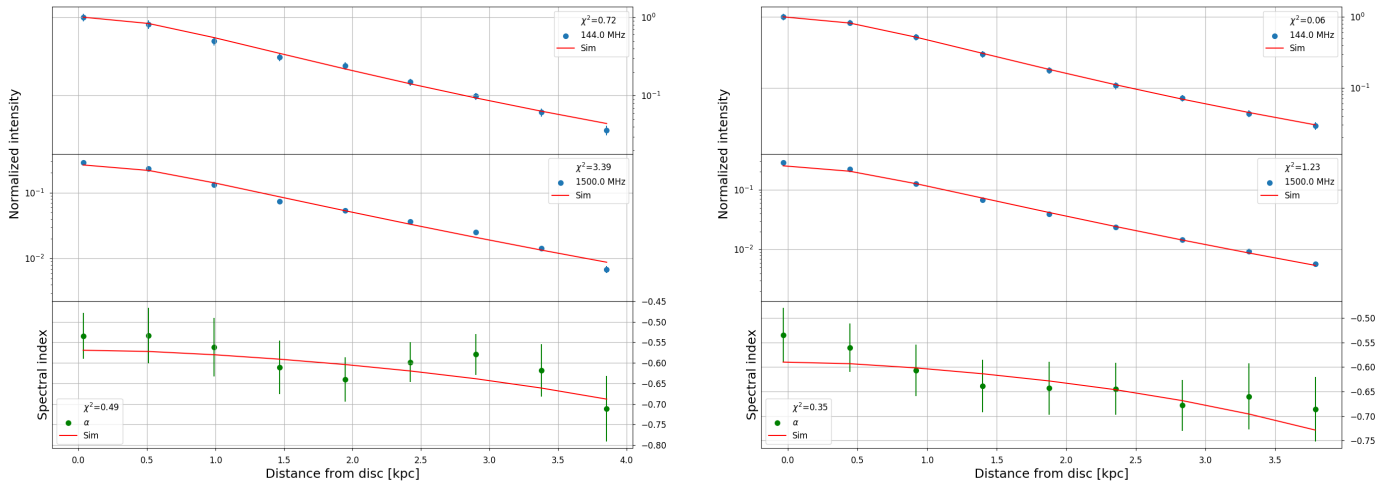
Fig. C.2. SPINNAKER profiles of NGC 3432 (all advection). Strips are presented as follows: left: LM and right: UM.
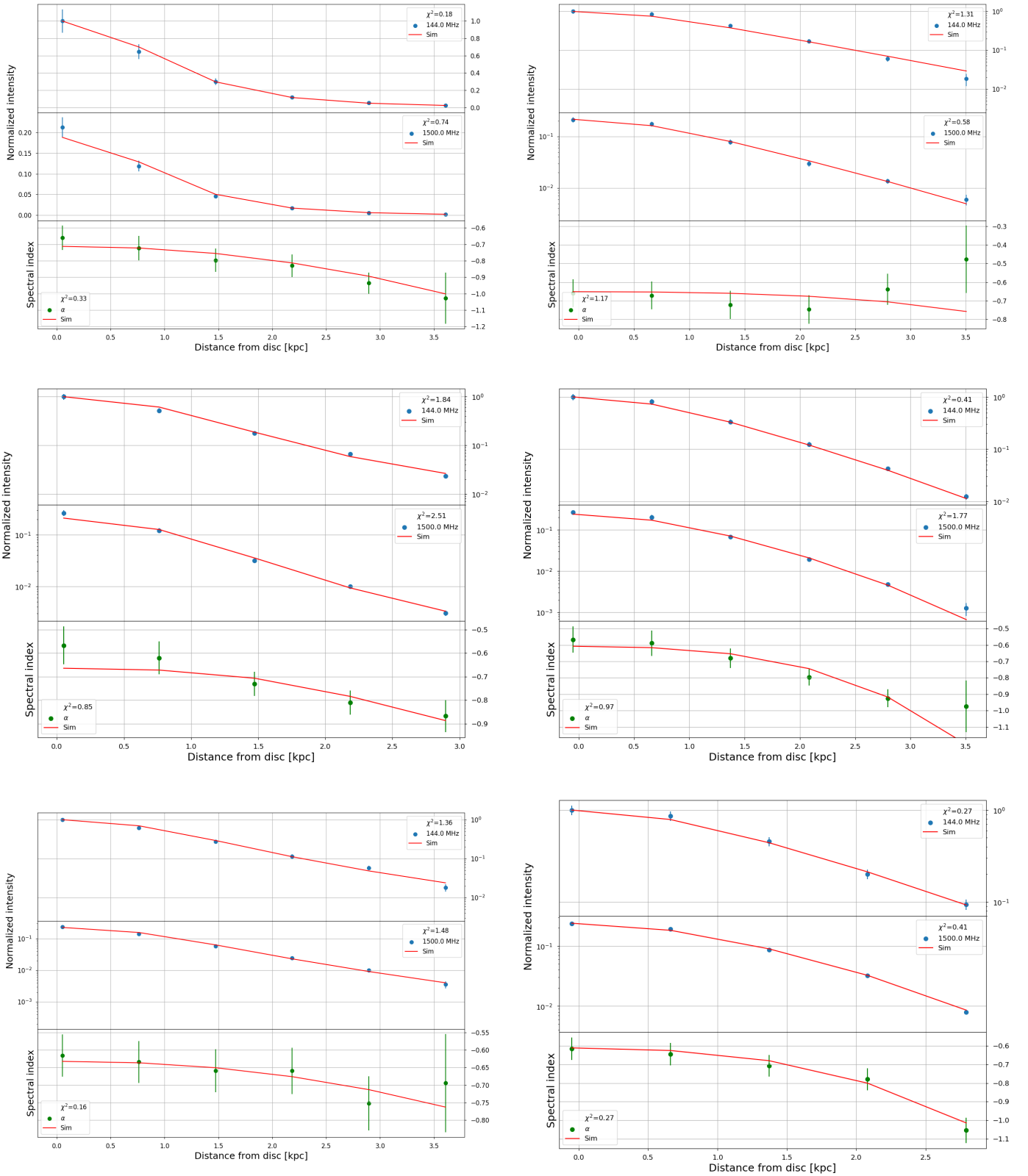
Fig. C.3. `SPINNAKER` profiles of NGC 4013. Strips are presented as follows: top left: LR (advection), top right: UR (diffusion), middle left: LM (advection), middle right: UM (diffusion), bottom left: LL (advection), and bottom right: UL (diffusion).
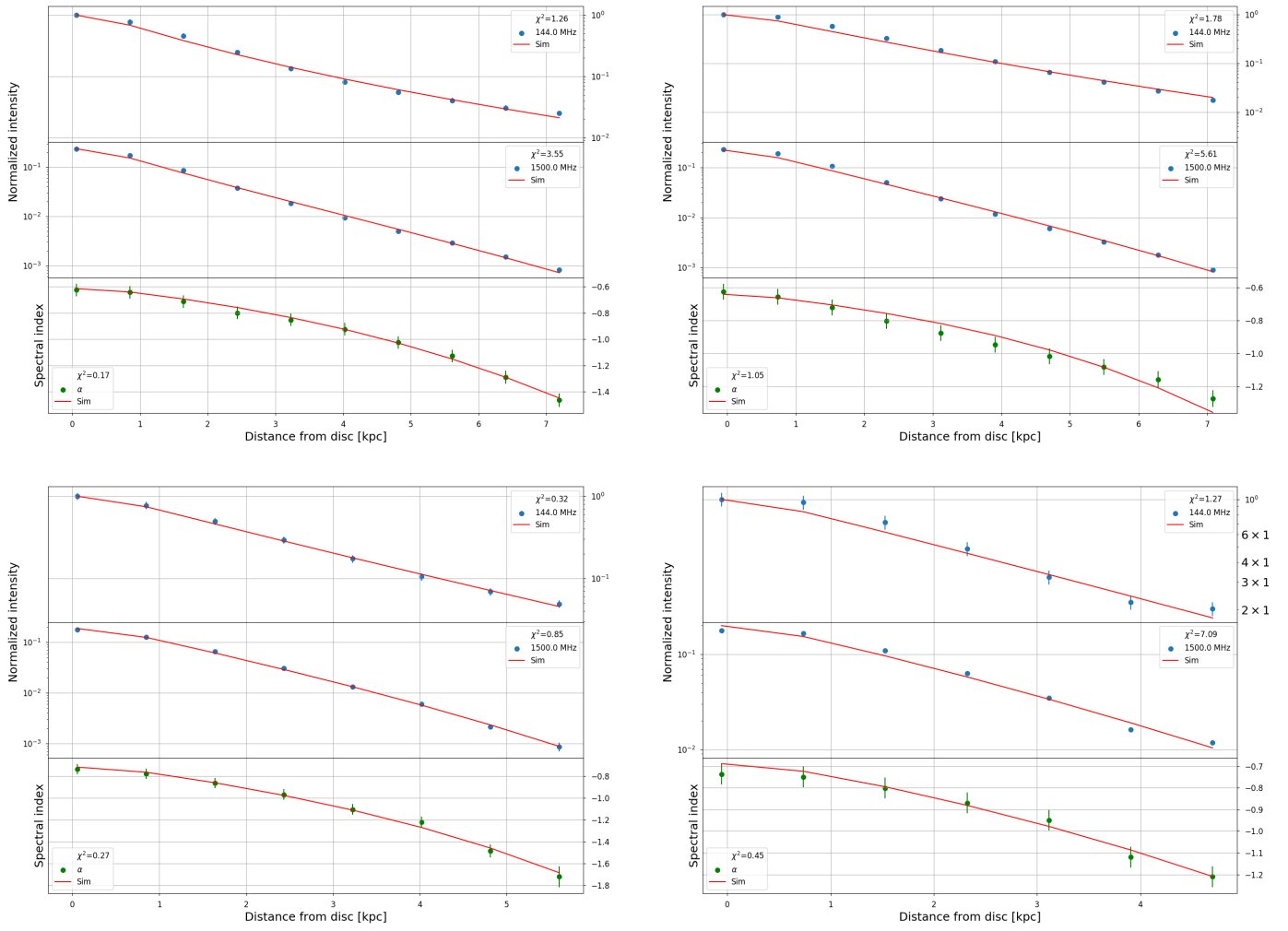
Fig. C.4. SPINNAKER profiles of NGC 4157 (all advection). Stripes are present as follows: top left: LM, top right: UM, bottom left: LL, and bottom right: UL.
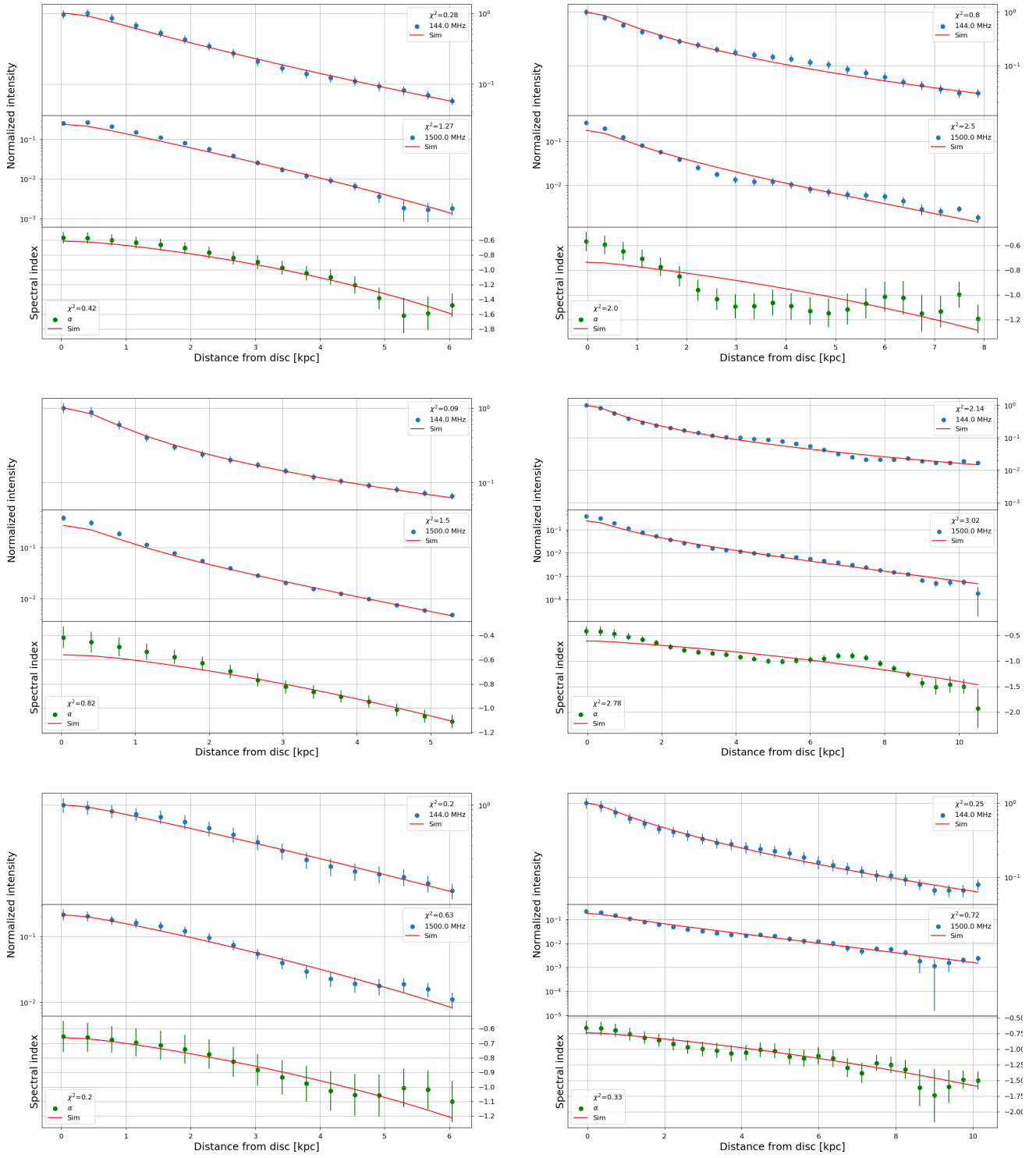
Fig. C.5. SPINNAKER profiles of NGC 4631 (all advection). Strips are presented as follows: top left: LR, top right: UR, middle left: LM, middle right: UM, bottom left: LL, and bottom right: UL.